



# Anisotropic density growth of bone—A computational micro-sphere approach

Tobias Waffenschmidt<sup>a,\*</sup>, Andreas Menzel<sup>a,b</sup>, Ellen Kuhl<sup>c,d</sup>

<sup>a</sup> Institute of Mechanics, Department of Mechanical Engineering, TU Dortmund, Leonhard-Euler-Str. 5, D-44227 Dortmund, Germany

<sup>b</sup> Division of Solid Mechanics, Lund University, P.O. Box 118, SE-22100 Lund, Sweden

<sup>c</sup> Center of Mechanics, Department of Mechanical Engineering, ETH Zurich, Tannenstrasse 3, CH-8092 Zurich, Switzerland

<sup>d</sup> Departments of Mechanical Engineering, Bioengineering, and Cardiothoracic Surgery, Stanford University, 496 Lomita Mall, Stanford, CA 94305, USA

## ARTICLE INFO

### Article history:

Received 18 August 2011

Received in revised form 24 February 2012

Available online 13 April 2012

### Keywords:

Adaptation

Remodelling

Anisotropic growth

Micro-sphere

Finite element method

## ABSTRACT

Bones are able to adapt their local density when exposed to mechanical loading. Such growth processes result in densification of the bone in regions of high loading levels and in resorption of the material in regions of low loading levels. This evolution and optimisation process generates heterogeneous distributions of bone density accompanied by pronounced anisotropic mechanical properties. While several constitutive models reported in the literature assume the growth process to be purely isotropic, only few studies focus on the modelling and simulation of anisotropic functional adaptation we can observe in vivo. Some of these few computational models for anisotropic growth characterise the evolution of anisotropy by analogy to anisotropic continuum damage mechanics while others include anisotropic growth but assume isotropic elastic properties.

The objective of this work is to generalise a well-established framework of energy-driven isotropic functional adaptation to anisotropic microstructural growth and density evolution. We adopt the so-called micro-sphere concept, which proves to be extremely versatile and flexible to extend sophisticated one-dimensional constitutive relations to the three-dimensional case. In this work we apply this framework to the modelling and simulation of anisotropic functional adaptation by means of a directional density distribution, which evolves in time and in response to the mechanical loading condition. Several numerical studies highlight the characteristics and properties of the anisotropic growth model we establish. The formulation is embedded into an iterative finite element algorithm to solve complex boundary value problems. In particular, we consider the finite-element-simulation of a subject-specific proximal tibia bone and a comparison to experimental measurements. The proposed model is able to appropriately represent the heterogeneous bone density distribution. As an advantage over several other computational growth models proposed in the literature, a pronounced local anisotropy evolution is identified and illustrated by means of orientation-distribution-type density plots.

© 2012 Elsevier Ltd. All rights reserved.

## 1. Motivation

The tibia is the strongest weight bearing bone in the body, and the second largest bone of the human skeleton. Although it plays a critical role in osteoarthritis—the most prevalent joint disorder in the world—the tibia remains much less well studied than other long bones; see, for instance, Hulet et al. (2002). Since the seminal work by Julius Wolff (1892), we know that long bones can adapt their local density to mechanical loading. During normal walking, for example, a majority of the generated load is transmitted through the medial side of the knee as reported by Baliunas et al. (2002). As a result, the bone mineral density of the tibia is typically significantly larger in the medial than in the lateral regions, see Hurwitz et al. (1998).

Fig. 1(a) illustrates the *isotropic functional adaption* in the healthy proximal tibia characterised through a Dual-Energy X-ray Absorptiometry scan. The different grey scales indicate the heterogeneous bone density distribution with a characteristic dense region in the medial plateau, a less dense region in the lateral plateau, and a low density in the central region, see the recent publication by Pang et al. (2012). Dual-Energy X-ray Absorptiometry is currently the most common diagnostic tool to quantify bone mineral density profiles. However, it fails to visualise microstructural anisotropy, a characteristic feature of spongy bone that has been recognised more than a century ago by von Meyer (1867). Fig. 1(b) displays the *anisotropic functional adaption* in the healthy proximal tibia characterised by a photograph of a thin frontal longitudinal section of the bone taken from Wolff (1870). It clearly documents the alignment of the trabecular architecture with the directions of maximum principal loading as, for instance, reported by Carter and Beaupré (2001).

\* Corresponding author. Tel.: +49 231 755 3567; fax: +49 231 755 2688.

E-mail address: [tobias.waffenschmidt@udo.edu](mailto:tobias.waffenschmidt@udo.edu) (T. Waffenschmidt).

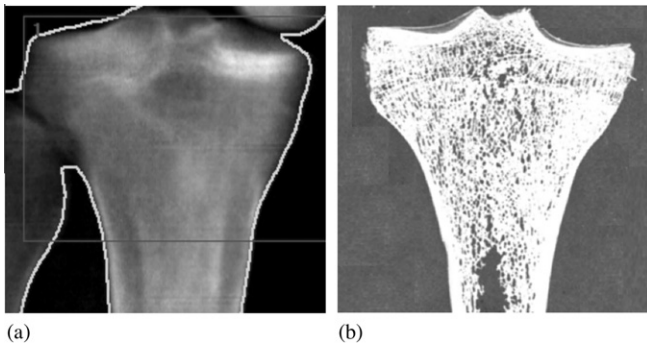


**Fig. 1.** Healthy proximal tibia. (a) Isotropic density distribution visualised through a Dual-Energy X-ray Absorptiometry scan of the proximal tibia. The scan displays the characteristic heterogeneous density distribution, with a dense region in the medial plateau, a lower density region in the lateral plateau, and the lowest density in the central region, cf. Pang et al. (2012). (b) Anisotropic density distribution visualised through a thin section of the proximal tibia. The photograph displays the microstructural arrangement of the trabeculae aligned with the axis of maximum principal loading, cf. Wolff (1870).

In the mid 1970s, biomechanical engineers have proposed the first mechanistic models to characterise the *isotropic functional adaptation* of bone in response to mechanical loading, see Carter and Hayes (1977), Cowin and Hegedus (1976) and Cowin and Doty (2007). These approaches model bone growth within the framework of open system thermodynamics, as discussed by Kuhl and Steinmann (2003a), using an enhanced balance of mass which allows bone to adapt its density driven by stress, strain or energy; see Himpel et al. (2005) and Kuhl and Steinmann (2003a) among others. Within the past two decades, we have recognised finite element analysis as a powerful tool to investigate the isotropic functional adaptation in the form of regional variations in density profiles, see Ambrosi et al. (2011) and Huiskes et al. (1987). As discussed in a comparative overview by Kuhl et al. (2003), finite element algorithms for growing tissue typically introduce the density as nodal degree of freedom (Jacobs et al., 1995; Kuhl and Steinmann, 2004), as internal variable (Harrigan and Hamilton, 1992), or local degree of freedom, which can be condensed on the element level (Beaupré et al., 1990). Finite element models allow us to predict bone growth and resorption in response to virtually any loading scenario, which would not be feasible experimentally, see Reina-Romo et al. (2010) or Weinans et al. (1992). They also allow for efficient parametric studies to identify key contributors to bone straightening (Carpenter and Carter, 2010), bone torsion (Taylor et al., 2009), or bone failure (Gitman et al., 2010; Zhang et al., 2010).

While the initial growth models for hard biological tissues are exclusively isotropic and fail to reproduce the characteristic microstructural architecture of spongy bone, only few studies focus on the *anisotropic functional adaptation* we can observe in vivo, as reported by Taber (1995). Most of the models proposed are directly motivated by the so-called ‘trajectorial hypothesis’ introduced by Wolff (1892) which states that—in addition to the change in apparent density of the bone tissue resulting from the growth and remodelling process—we also observe a time-dependent alignment of the trabecular architecture with the directions of maximum principal loading directions, in other words anisotropy evolution. To give a short overview, we subsequently briefly describe different anisotropic bone remodelling approaches—the list of related references, however, not being claimed to be exhaustive.

As one of the first contributions on anisotropic bone remodelling considered here, Carter et al. (1989) introduced a mathematical formulation for the functional adaptation of trabecular bone. The formulation is based on a self-optimisation concept, which takes into account the influence of different load cases weighted

by the corresponding number of load cycles. For a single load case it is discussed that an alignment of the principal material axes with the principal stress axes will result in an optimal material microstructure orientation in the context of local stiffness maximisation. Almost a decade later, Jacobs et al. (1997) proposed to add a remodelling rule for the rate-of-change of the full anisotropic elasticity tensor to the density rate-of-change rule adapted from an existing isotropic remodelling theory. In a review paper on existing bone remodelling formulations, Pettermann et al. (1997) discussed a micro-macro mechanical description of bone in its different microstructural configurations and derived a remodelling algorithm accompanied by a new unified material model for describing the linear elastic orthotropic behaviour of bone. Based on a hypo-elastic material model, Weng (1998) made use of a formulation which—conceptually similar to Jacobs et al. (1997)—assumed an evolution of the stiffness tensor. Inspired by mathematical optimisation approaches, Fernandes et al. (1999) and Rodrigues et al. (2002) proposed an analytical parametric microstructural model from which a global material model was obtained by making use of homogenisation concepts. An optimal material structure constructed by means of homogenised material properties could be found by optimising a cost function. This cost or rather goal function accounts for both, the structural stiffness and the biological costs associated with metabolic maintenance of the bone tissue. In a series of papers, Doblaré and García (2002) introduced internal remodelling from general damage-repair theories adopting the framework of continuum damage mechanics. In these works a damage-repair-tensor is defined in terms of the apparent density and a fabric tensor is associated with the porosity and directionality of the trabeculae; see also Cowin (1985, 1986) or Zysset and Curnier (1995). In a follow-up paper García et al. (2001) considered also external remodelling, whereas a subsequent contribution analysed the proximal femur before and after total hip replacement, Doblaré and García (2002). Similar to the contributions above, Nackenhörst et al. (2000) and Krstin et al. (2000) made use of a fabric tensor description for porous materials to extend the isotropic theory to anisotropic material behaviour. In some recent publications, Coelho et al. (2008) and Coelho et al. (2009) proposed a hierarchical model based on the above mentioned topology-optimisation-related approaches to model the bone apparent density distribution at the macro scale and the trabecular structure at the micro scale. Bone at global macroscopic scale is consequently assumed as a continuum characterised by equivalent or rather homogenised material properties.

In the present contribution we adopt a conceptually different approach. We generalise the well-established format of isotropic functional adaptation by Harrigan and Hamilton (1994) to microstructural anisotropy using the micro-sphere concept—also denoted as micro-plane formulation—as originally introduced by Bažant and Oh (1985). Creating an anisotropic representation through the integration of one-dimensional constitutive equations over the unit sphere, cf. Bažant and Oh (1986), the micro-sphere approach is extremely versatile and flexible to incorporate inelasticity in the form of damage or plasticity at small strains, see Kuhl et al. (2001, 2000), or large strains as, for instance, applied to rubber-like materials, see the series of papers by Miehe et al. (2004), Miehe and Göktepe (2005) and Göktepe and Miehe (2005), or collagenous tissues, see Alastrué et al. (2009) and Alastrué et al. (2009). By assigning deformation-driven evolution equations for different orientations, as discussed in Menzel (2007) and Himpel et al. (2008), recent attempts have also used the micro-sphere concept to characterise the mechanically-driven reorientation of microstructural directions in soft biological tissues or in the context of structural design; see Menzel and Waffenschmidt (2009), Menzel et al. (2010) and Waffenschmidt and Menzel (2012). We utilise the micro-sphere concept to characterise the anisotropic

functional adaptation through directional densities which evolve in response to directional energies. We illustrate the energy-driven evolution of anisotropy using zeroth, second and fourth order fabric tensors or rather density moments, cf. Kanatani (1984) and Menzel and Waffenschmidt (2009).

The paper is organised as follows. In Section 2, we briefly summarise relevant kinematic, kinetic and balance relations for bone growth within open system thermodynamics. Next, in Section 3, we discuss the model problem of one-dimensional energy-driven density growth in terms of its constitutive equations, its implementation and an illustrative example. In Section 4, we generalise the one-dimensional formulation to a three-dimensional setting using the micro-sphere concept and study a homogeneous model problem. Last, in Section 5, we embed the three-dimensional equations for anisotropic energy-driven density growth into a finite element framework to explore the isotropic density distribution and the anisotropic microstructure in the proximal tibia. We conclude with a summary and final remarks in Section 6.

## 2. Basic kinematics and balance equations

Let  $\mathbf{x} = \boldsymbol{\varphi}(\mathbf{X}, t)$  describe the motion of the body, which transforms referential position vectors of material particles  $\mathbf{X}$  to their spatial counterparts  $\mathbf{x}$ . Moreover, the deformation gradient and the right Cauchy-Green deformation tensor are denoted by

$$\mathbf{F} = \nabla_{\mathbf{X}} \boldsymbol{\varphi}, \quad \mathbf{C} = \mathbf{F}^t \cdot \mathbf{F}, \quad (1)$$

with the Jacobian  $J = \det(\mathbf{F}) > 0$ . In view of the material model discussed in the sequel, we introduce the stretch in the direction of the unit-vector  $\mathbf{r}$ , i.e.,

$$\lambda = \sqrt{\mathbf{r} \cdot \mathbf{C} \cdot \mathbf{r}}. \quad (2)$$

Even though bone tissue commonly experiences small strains within the physiological deformation range, we make use of a finite strain formulation for the sake of generality. As a special case of large strain, the small strain framework is included. The large strain formulation, however, proves to be natural to include different responses in tension and compression, see also Fig. 2. Computationally, a large strain formulation comes at almost no extra cost, since the overall set of equations is nonlinear anyways.

As this work proceeds, we consider growth phenomena that are exclusively related to changes in referential density  $\rho_0 = J\rho_t$ , which can be described by means of the mass balance equation

$$\dot{\rho}_0 = \nabla_{\mathbf{X}} \cdot \mathbf{R} + R_0, \quad (3)$$

with  $(\dot{\bullet})$  denoting the material time derivative. The mass flux  $\mathbf{R}$  is assumed to vanish, i.e.,  $\nabla_{\mathbf{X}} \cdot \mathbf{R} = 0$ , such that the mass source  $R_0$  coincides with the rate of referential density  $\dot{\rho}_0 = R_0$ . For the sake of conceptual simplicity, we do not consider a dead-zone as proposed by, for instance, Weinans et al. (1992).

## 3. One-dimensional growth

This section reviews basic aspects of the constitutive relations of density growth, where we restrict ourselves to a one-dimensional setting. The one-dimensional theoretical and computational framework provides the basic model for the anisotropic micro-sphere-based growth model proposed in Section 4. We discuss key aspects of the numerical implementation and investigate specific properties of the underlying constitutive model. We refer to Kuhl and Steinmann (2003b) and Menzel (2005) for details concerning the underlying constitutive theory whereas in Jacobs et al. (1995), Kuhl et al. (2003) and Kuhl and Steinmann (2003a) additional background information on algorithmic aspects is elaborated further.

### 3.1. Constitutive equations

Following Harrigan and Hamilton (1993b), we adopt a constitutive relation for the mass source,

$$R_0 := k_\rho^* \left[ \frac{\rho_0}{\rho_0^*} \right]^{-m^*} \psi_0 - \psi_0^*, \quad (4)$$

which, combined with the definition of the mass source  $\dot{\rho}_0 = R_0$ , yields the evolution of the density as

$$\dot{\rho}_0 = k_\rho^* \left[ \frac{\rho_0}{\rho_0^*} \right]^{-m^*} \psi_0 - \psi_0^*. \quad (5)$$

Herein,  $\psi_0$  denotes a relative density-scaled strain energy per unit volume,  $\rho_0^*$  is the initial density and  $\psi_0^* = \text{const}$  takes the representation of an energy-type saturation value for the density evolution. Finally,  $k_\rho^*$  characterises the rate of density evolution and  $m^*$  is an algorithmic exponent ensuring the stability of the algorithm, see Harrigan and Hamilton (1993a). Table 1 summarises the essential quantities together with their units, wherein quantities associated with superscript  $(\bullet)^*$  denote material parameters.

Using these considerations, we express the strain energy per unit volume  $\psi_0$  as

$$\psi_0 = \left[ \frac{\rho_0}{\rho_0^*} \right]^{n^*} \psi_0^e(\lambda), \quad (6)$$

wherein  $\psi_0^e$  is a hyperelastic strain energy function in one-dimensional form and  $n^*$  denotes a dimensionless porosity exponent depending on the particular open-pored ground substance, see Harrigan and Hamilton (1993a). The Piola-Kirchhoff stress takes the representation

$$S = 2 \frac{\partial \psi_0}{\partial \lambda^2} = \left[ \frac{\rho_0}{\rho_0^*} \right]^{n^*} S^e \quad \text{with} \quad S^e = \frac{1}{\lambda} \frac{\partial \psi_0^e}{\partial \lambda}. \quad (7)$$

The strain energy  $\psi_0$  as well as the stress  $S$  are determined by the density-independent quantities  $\psi_0^e$  and  $S^e = 2 \partial \psi_0^e / \partial \lambda^2$ , respectively, weighted by a relative density power,  $[\rho_0 / \rho_0^*]^{n^*}$ , where  $m^* > n^*$  in order to ensure numerical stability or rather density saturation, see Harrigan and Hamilton (1992).

### 3.2. Implementation

The evolution equation (5) represents a nonlinear ordinary differential equation, which, in connection with Eq. (6), reads

$$\dot{\rho}_0 = k_\rho^* \left[ \frac{\rho_0}{\rho_0^*} \right]^{n^* - m^*} \psi_0^e - \psi_0^*. \quad (8)$$

We apply a numerical integration scheme in order to obtain the density at a current time step. Consequently, we introduce respective intervals in time,  $\Delta t = t_{n+1} - t_n \geq 0$ , and apply an implicit Euler backward integration scheme,

$$\rho_0 = \rho_{0n} + \Delta t \dot{\rho}_0 \quad \text{with} \quad \rho_0|_{t_0} = \rho_0^*. \quad (9)$$

Here and in the following, we omit the subscript index  $n+1$  associated with time  $t_{n+1}$  for the sake of readability. The related residual form then reads

$$r_\rho(\rho_0) = \rho_0 - \rho_{0n} - \Delta t \dot{\rho}_0 = 0. \quad (10)$$

To solve this non-linear equation we suggest a Newton iteration scheme. We expand Eq. (10) in a Taylor series at  $\rho_0^k$  with  $k$  denoting the particular Newton iteration step. Neglecting terms of second and higher order, we obtain

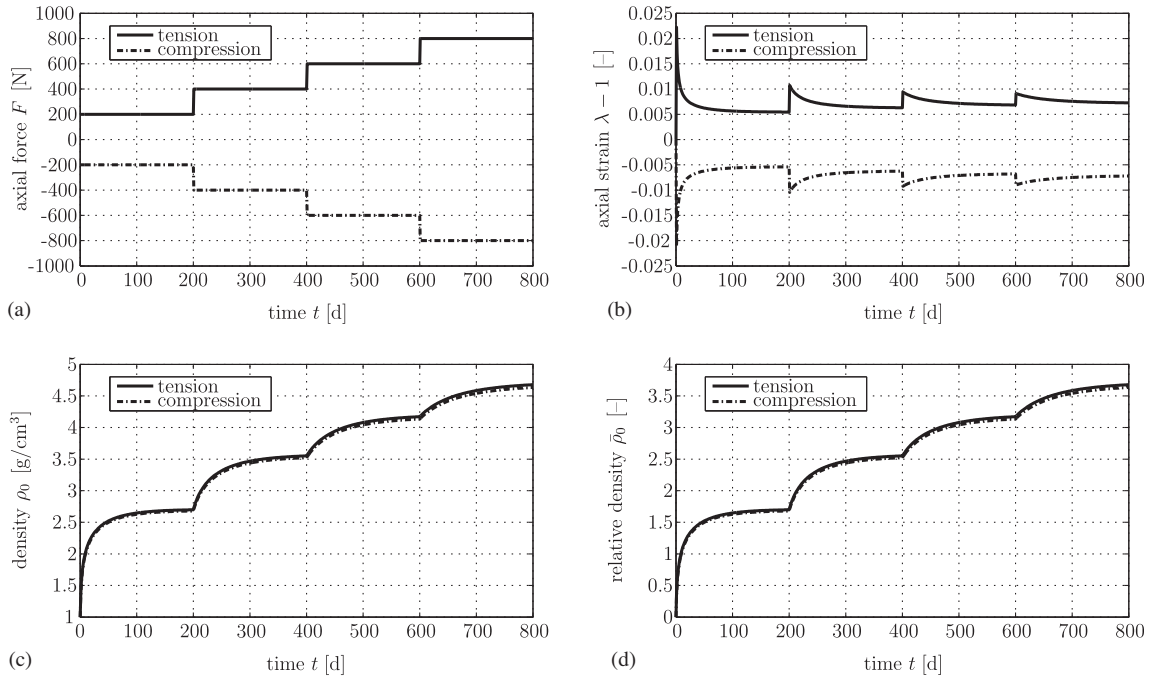


**Fig. 2.** Response of the one-dimensional density growth model. (a) Stepwise constant tensile and compressive loading in terms of the axial force  $F$ . (b–d) Evolution of strain  $\lambda-1$ , density  $\rho_0$  and relative density  $\bar{\rho}_0 = [\rho_0 - \rho_0^k]/\rho_0^k$  with respect to time for the material parameters given in Table 3.

**Table 1**  
Quantities included in constitutive relations (4) and (5).

Quantity	Description	Unit (SI)
$R_0$	Mass source	[kg/m <sup>3</sup> s]
$\rho_0$	Density	[kg/m <sup>3</sup> ]
$\rho_0^k$	Initial density	[kg/m <sup>3</sup> ]
$\psi_0$	Strain energy	[J/m <sup>3</sup> ]
$\psi_0^*$	Saturation value	[J/m <sup>3</sup> ]
$k_\rho^*$	Density evolution (growth) velocity	[d/m <sup>2</sup> ]
$m^*$	Algorithmic exponent	[-]
$n^*$	Porosity exponent	[-]

$$r_\rho(\rho_0^k) + \frac{\partial r_\rho(\rho_0)}{\partial \rho_0} \Big|_{\rho_0^k} [\rho_0 - \rho_0^k] = 0 \quad (11)$$

and introduce the increment of the referential density as

$$\Delta \rho_0 = \rho_0^{k+1} - \rho_0^k = - \left[ \frac{\partial r_\rho(\rho_0)}{\partial \rho_0} \Big|_{\rho_0^k} \right]^{-1} r_\rho(\rho_0^k). \quad (12)$$

The remaining task now consists in deriving the partial derivative of the residual  $r_\rho(\rho_0)$  with respect to the density at the current time step  $\rho_0$ , which yields

$$\frac{\partial r_\rho(\rho_0)}{\partial \rho_0} \Big|_{\rho_0^k} = 1 - \Delta t \frac{\partial \dot{\rho}_0^k}{\partial \rho_0^k}. \quad (13)$$

The derivative of the density evolution with respect to the density itself follows from Eq. (8),

$$\frac{\partial \dot{\rho}_0^k}{\partial \rho_0^k} = [n^* - m^*] \frac{k_\rho^*}{\rho_0^k} \left[ \frac{\rho_0^k}{\rho_0^*} \right]^{n^* - m^*} \psi_0^e. \quad (14)$$

We end up with the algorithmic update of the density

$$\rho_0^{k+1} = \rho_0^k + \Delta \rho_0, \quad (15)$$

which must be evaluated iteratively as long as the norm of the residual is larger than a pre-defined tolerance.

In case of a one-dimensional force- or rather stress-driven tension/compression test, which is typically accompanied by an iterative procedure in order to calculate the equilibrium configuration, we determine the algorithmic tangent operator,

$$E = 2 \frac{dS}{d\lambda^2} = E_\lambda + E_{\rho_0}, \quad (16)$$

By means of the chain rule, we identify the two contributions as

$$E_\lambda = 2 \frac{\partial S}{\partial \lambda} \frac{\partial \lambda}{\partial \lambda^2} \quad \text{and} \quad E_{\rho_0} = 2 \frac{\partial S}{\partial \rho_0} \frac{\partial \rho_0}{\partial \lambda^2}, \quad (17)$$

wherein the first term represents the elastic moduli and the second term reflects the dependence of the density evolution equation (5) on the deformation via the strain energy function  $\psi_0$ .

The first contribution  $E_\lambda$  can be determined straightforwardly as the elastic tangent modulus  $E^e = 2 \partial^2 S^e / \partial \lambda^2$  weighted by the relative density power,  $[\rho_0 / \rho_0^*]^{n^*}$ , i.e.,

$$E_\lambda = \left[ \frac{\rho_0}{\rho_0^*} \right]^{n^*} E^e \quad \text{with} \quad E^e = \frac{1}{\lambda^2} \left[ \frac{\partial^2 \psi_0^e}{\partial \lambda \partial \lambda} - \frac{1}{\lambda} \frac{\partial \psi_0^e}{\partial \lambda} \right]. \quad (18)$$

The density-related contribution  $E_{\rho_0}$  can directly be obtained by the partial derivative of  $S$  with respect to  $\rho_0$  as

$$\frac{\partial S}{\partial \rho_0} = \frac{n^*}{\rho_0} \left[ \frac{\rho_0}{\rho_0^*} \right]^{n^*} S^e. \quad (19)$$

We can compute the second term by means of the derivative of Eq. (10) with respect to  $\lambda^2$  and solving for  $\partial \rho_0 / \partial \lambda^2$  which results in

$$\frac{\partial \rho_0}{\partial \lambda^2} = \Delta t \left[ 1 - \Delta t \frac{\partial \dot{\rho}_0}{\partial \rho_0} \right]^{-1} \frac{\partial \dot{\rho}_0}{\partial \lambda^2} \quad (20)$$

with

$$\frac{\partial \dot{\rho}_0}{\partial \lambda^2} = \frac{k_\rho^*}{2} \left[ \frac{\rho_0}{\rho_0^*} \right]^{n^* - m^*} S^e. \quad (21)$$

In summary, the density-related contribution  $E_{\rho_0}$  of the algorithmic tangent operator takes the representation

$$\mathbb{E}_{\rho_0} = \frac{1}{\lambda^2} \left[ \frac{\rho_0}{\rho_0^*} \right]^{n^*} \left[ \frac{\Delta t n^* k_p^*}{\rho_0^*} \left[ 1 - \Delta t \frac{\partial \dot{\rho}_0}{\partial \rho_0} \right]^{-1} \left[ \frac{\rho_0}{\rho_0^*} \right]^{n^* - m^*} \left[ \frac{\partial \psi_0^e}{\partial \lambda} \right]^2 \right]. \quad (22)$$

The algorithm related to the constitutive model is summarised in Table 2.

### 3.3. Numerical example

To complete the constitutive model, we specify the particular type of the strain energy and assume a compressible neo-Hookean format,

$$\psi_0^e(\lambda) = \frac{\lambda^*}{2} \ln^2(\lambda) + \frac{\mu^*}{2} [\lambda^2 - 1 - 2 \ln(\lambda)]. \quad (23)$$

Based on this, we evaluate the derivatives of the free energy  $\psi_0^e$  with respect to the stretch  $\lambda$  as

$$\frac{\partial \psi_0^e}{\partial \lambda} = \frac{1}{\lambda} [\lambda^* \ln(\lambda) + \mu^* [\lambda^2 - 1]] \quad (24)$$

and

$$\frac{\partial^2 \psi_0^e}{\partial \lambda \partial \lambda} = \frac{1}{\lambda} \left[ \frac{\lambda^*}{\lambda} + 2\mu^* \lambda - \frac{\partial \psi_0^e}{\partial \lambda} \right]. \quad (25)$$

In view of the material parameters, we adopt the values calibrated by Pang et al. (2012) for the tibia, as summarised in Table 3 and set the time step size to  $\Delta t = 1.0$  [d]. The tolerance for the local Newton-scheme is  $\text{tol} = 10^{-8}$ .

To discuss the constitutive behaviour characteristic for density evolution, we consider a one-dimensional homogeneous tension–compression test. External loading is applied stepwise in terms of the axial force  $F$  and a stress-driven formulation is chosen as shown in Fig. 2(a). We preferably adopt realistic force magnitudes up to 800 [N] corresponding to the deformation levels obtained in Section 5 later on where we elaborate finite-element-based simulations of a tibia.

Fig. 2(b–d) show the temporal evolution of strain  $\lambda - 1$ , density  $\rho_0$  and relative density  $\bar{\rho}_0 = [\rho_0 - \rho_0^*] / \rho_0^*$ . Due to the stepwise application of constant forces and with regard to the resulting strain in Fig. 2(b), we observe a distinct time-dependent behaviour, whereas in Figs. 2(c, d) the (relative) density saturates in a viscous manner towards the so-called biological equilibrium state. The biological equilibrium state depends on the particular loading conditions and can be understood as the state where the deformations and the density remain constant for a given load, i.e.,  $\dot{\rho}_0 = 0$  and  $\dot{\lambda} = 0$ . For the chosen loading conditions, in connection with the chosen material parameters, the density increases monotonically with time from one loading level to the next higher loading level. In general, the density may also decrease at lower loading levels as shown in Fig. 3(b) later on. We observe that the model naturally captures different material response under tension and compression—the density evolution calculated for tension and compression does not coincide exactly. This effect is caused by the typical tension–compression–asymmetry of the neo-Hookean free energy function which, apparently, becomes more pronounced with increasing levels of deformation. In order to further emphasise this asymmetry, we could incorporate additional modifications of the strain energy function, e.g., by means of strain-related sign-type contributions, which, however, are not considered as this work proceeds.

Furthermore, we investigate the sensitivity of the constitutive response with respect to the material parameters, see Fig. 3. In order to additionally include resorption effects, we use the loading history displayed in Fig. 2(a) but reduce the magnitude of the force to  $F/10$ . Fig. 3(a) shows the influence of the initial density  $\rho_0^*$ . Even though not directly obvious from evolution equation (5), the initial density governs the rate of density evolution—higher initial values

**Table 2**

Constitutive box for the one-dimensional density-evolution-based growth model.

0. given deformation in terms of the stretch  $\lambda$  at time  $t_{n+1}$  and history data  $\rho_{0n}$  of internal density variables at time  $t_n$
1. compute density-independent elastic strain energy  $\psi_0^e$
2. perform local Newton iteration
  - (a) compute density residual

$$r_\rho = \rho_0 - \rho_{0n} - \Delta t k_p^* \left[ \frac{\rho_0}{\rho_0^*} \right]^{n^* - m^*} \psi_0^e - \psi_0^*$$

- (b) compute linearisation of residual

$$\frac{\partial \dot{\rho}_0}{\partial \rho_0} = [n^* - m^*] \frac{k_p^*}{\rho_0} \left[ \frac{\rho_0}{\rho_0^*} \right]^{n^* - m^*} \psi_0^e$$

- (c) compute density update

$$\rho_0 \leftarrow \rho_0 + \left[ \Delta t \frac{\partial \dot{\rho}_0}{\partial \rho_0} + 1 \right]^{-1} r_\rho$$

- (d) check tolerance

if  $|r_\rho| < \text{tol}$  go to 3.  
else go to 2. (a)

3. compute density weighted Piola–Kirchhoff stress and tangent operator (one-dimensional case: E necessary only in case of a stress-driven algorithm)

$$S = \frac{1}{\lambda} \left[ \frac{\rho_0}{\rho_0^*} \right]^{n^*} \frac{\partial \psi_0^e}{\partial \lambda}$$

$$E = \frac{1}{\lambda^2} \left[ \frac{\rho_0}{\rho_0^*} \right]^{n^*} [\bar{E}_\lambda + \bar{E}_{\rho_0}]$$

with

$$\bar{E}_\lambda = \frac{\partial^2 \psi_0^e}{\partial \lambda \partial \lambda} - \frac{1}{\lambda} \frac{\partial \psi_0^e}{\partial \lambda}$$

$$\bar{E}_{\rho_0} = \frac{\Delta t n^* k_p^*}{\rho_0^*} \left[ 1 - \Delta t \frac{\partial \dot{\rho}_0}{\partial \rho_0} \right]^{-1} \left[ \frac{\rho_0}{\rho_0^*} \right]^{n^* - m^*} \left[ \frac{\partial \psi_0^e}{\partial \lambda} \right]^2$$

**Table 3**

Set of material parameters used for the calculations, as calibrated by Pang et al. (2012).

Parameter	Value	Unit
$\lambda^*$	2186.0	[N/mm <sup>2</sup> ]
$\mu^*$	1458.0	[N/mm <sup>2</sup> ]
$\rho_0^*$	1.0	[g/cm <sup>3</sup> ]
$\psi_0^*$	0.0275	[N/mm <sup>2</sup> ]
$k_p^*$	0.4	[d/cm <sup>2</sup> ]
$n^*$	2.0	[-]
$m^*$	3.0	[-]

of  $\rho_0^*$  reduce the growth velocity but result in identical density equilibrium levels. The energy-type saturation or rather target value  $\psi_0^*$  essentially influences the level of the density at biological equilibrium. Reducing this parameter leads to a remarkable increase of the density level. However, as indicated above, increasing this parameter—depending on the particular loading level—may cause the material to degrade at lower loading levels as illustrated in Fig. 3(b, shaded region). The combination of the algorithmic parameter  $m^*$  and the porosity exponent  $n^*$  also affects the level and the rate of the density saturation, see Fig. 3(c). Note that only the difference  $n^* - m^*$  enters the density evolution equation (5). However, the curves of the relative density  $\bar{\rho}_0$  for the parameter-combinations  $n^* = 2, m^* = 3$  and  $n^* = 1, m^* = 2$ —so that  $n^* - m^* = -1$  in both cases—significantly deviate from one another. This observation is attributed to the present stress-driven

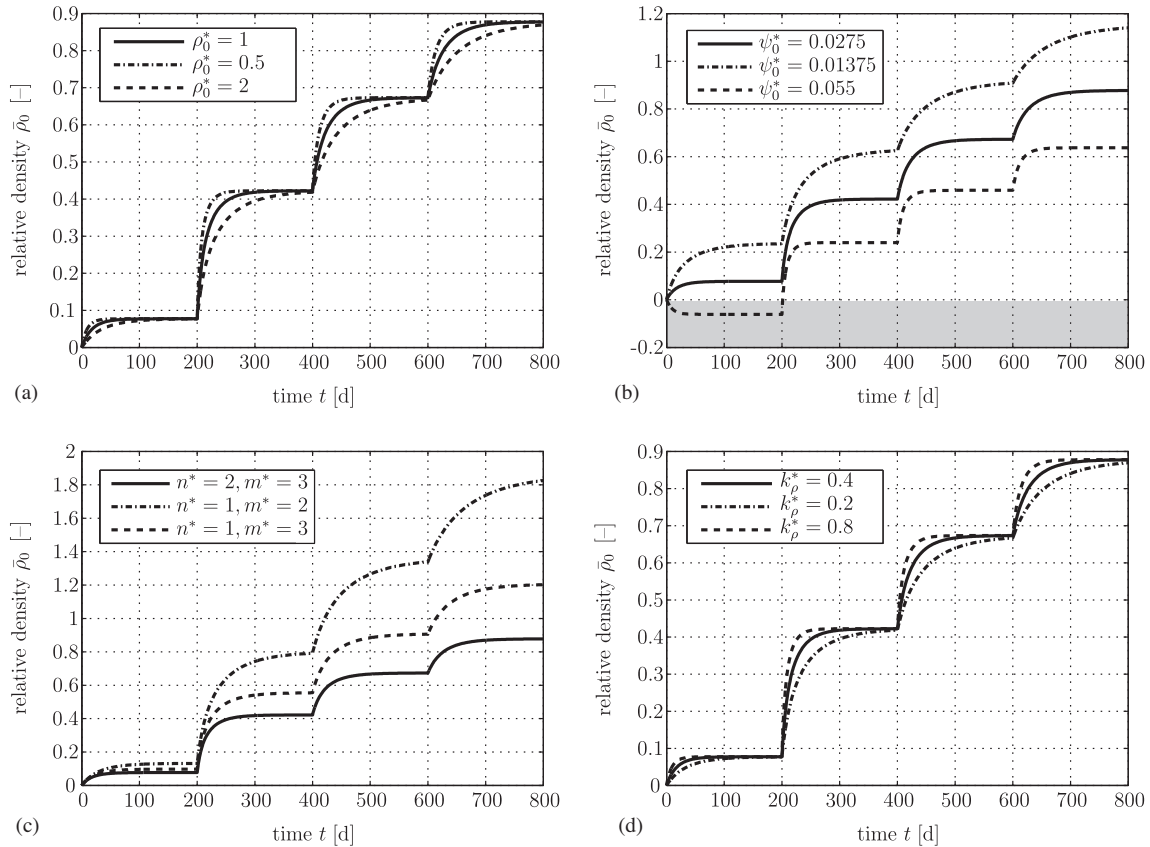


**Fig. 3.** Investigation of the sensitivity of the density response  $\bar{\rho}_0(t)$  for the loading history depicted in figure 2(a) with an axial force of magnitude  $F/10$ . The respective material parameters are modified as compared to the reference material data set given in Table 3; modifications: (a) initial density  $\rho_0$ , (b) energy-type saturation value  $\psi_0^*$ , (c) algorithmic parameters  $n^*$  and  $m^*$ , (d) growth velocity  $k_\rho^*$ .

loading, cf. Eq. (7), where the porosity exponent  $n^*$  enters the definition of the Piola–Kirchhoff stress. For a strain-driven process, however, these two curves in Fig. 3(c) would coincide. Finally,  $k_\rho^*$  governs the growth velocity as specified in Eq. (5).

#### 4. Anisotropic growth

This section deals with the extension of the one-dimensional density evolution model, discussed in the previous section, to the three-dimensional macroscopic level by means of a so-called micro-sphere formulation (also known as micro-plane formulation, as introduced by Bažant and Oh (1985)). One property of the proposed formulation is the inherent direction-dependent response which, in consequence, leads to an anisotropic model of growth by direction-dependent local density evolution. For alternative anisotropic growth models based on macroscopic continuum approaches, we refer to Jacobs et al. (1997) and Menzel (2005). Analogous micro-sphere approaches, including internal variables, are proposed by Göktepe and Miehe (2005) and Harrysson et al. (2010).

##### 4.1. Extension to a three-dimensional formulation—a micro-sphere approach

To obtain a fully three-dimensional constitutive model, we now expand the one-dimensional formulation of Section 2 using the micro-sphere concept. Conceptually speaking, the continuum approach is based on a one-dimensional constitutive equation. We extend this one-dimensional constitutive relation to the three-dimensional macroscopic level by means of an integration over the underlying unit-sphere  $\mathbb{U}^2$ . Characteristic for the algorithmic

implementation of this approach is a finite number of  $m$  unit-vectors  $\mathbf{r}_i$  to be considered for the numerical integration over the unit-sphere, by means of which we compute the macroscopic stress tensor and tangent operator.

In the present context of a micro-sphere model, macroscopic quantities per unit volume are represented by

$$\langle\langle \bullet \rangle\rangle = \frac{1}{4\pi} \int_{\mathbb{U}^2} (\bullet) \, dA, \quad (26)$$

which allows to rewrite the macroscopic strain energy function as

$$\Psi_0 = \langle \psi_0(\lambda) \rangle. \quad (27)$$

Herein,  $\psi_0$  denotes the one-dimensional strain energy function introduced in (6) and  $\lambda$  represents the stretch as defined in Eq. (2). Based on this and by analogy with Eq. (7), the macroscopic Piola–Kirchhoff stresses result in

$$\mathbf{S} = 2 \frac{\partial \Psi_0}{\partial \mathbf{C}} = 2 \left\langle \frac{\partial \psi_0}{\partial \lambda} \frac{\partial \lambda}{\partial \mathbf{C}} \right\rangle = \left\langle \left[ \frac{\rho_0}{\rho_0^*} \right]^{n^*} \mathbf{S}^e \right\rangle \quad (28)$$

including the elastic Piola–Kirchhoff stresses

$$\mathbf{S}^e = \mathbf{S}^e \mathbf{r} \otimes \mathbf{r} \quad (29)$$

weighted by the relative density power  $[\rho_0/\rho_0^*]^{n^*}$ , where we make use of the relation

$$\frac{\partial \lambda}{\partial \mathbf{C}} = \frac{1}{2\lambda} \mathbf{r} \otimes \mathbf{r}. \quad (30)$$

Application of Eq. (26) to the unit vectors  $\mathbf{r} \in \mathbb{U}^2$ , and higher order moments thereof, results in constraints such as  $\langle \mathbf{r} \rangle = \mathbf{0}$  and  $\langle \mathbf{r} \otimes \mathbf{r} \rangle = \frac{1}{3} \mathbf{I}$ , see also A.2.

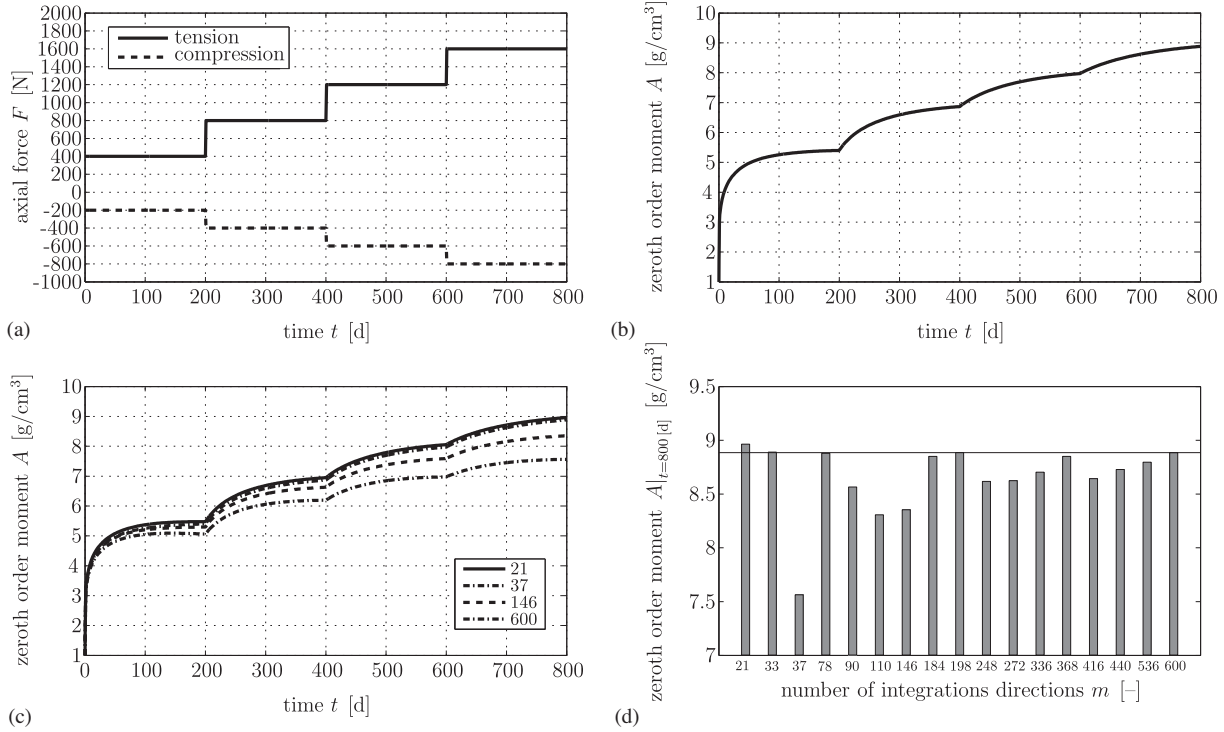


**Fig. 4.** Response of the three-dimensional density growth model for a combined homogeneous tension–compression test. (a) Stepwise constant tensile and compressive loading levels in terms of the axial forces  $F$  with  $F_{\text{tens}} = -2F_{\text{comp}}$ . (b) Evolution of zeroth-order moment  $A$  representing the macroscopic density using  $m = 21$  integration directions. (c) Comparison of zeroth-order moment  $A$  using four different integration schemes. (d) Comparison of the zeroth-order moment  $A|_{t=800[d]}$  for 17 different integrations schemes with a maximum number of  $m = 600$  integration directions per hemisphere.

## 4.2. Implementation

To integrate the constitutive equations over the unit sphere  $\mathbb{U}^2$ , we adopt  $m$  discrete integration direction vectors  $\mathbf{r}^i$  and introduce  $w^i$  as the related weighting factors. Accordingly, we approximate the continuous representation introduced in Eq. (27) by

$$\langle \langle \bullet \rangle \rangle = \frac{1}{4\pi} \int_{\mathbb{U}^2} \langle \bullet \rangle dA \approx \sum_{i=1}^m w^i \langle \bullet \rangle^i. \quad (31)$$

Several integration schemes over the unit-sphere of different approximation order have been studied in the literature. In this regard, we refer the reader also to Fig. 4(c,d) the corresponding comments made in Section 4.3, where we compare 17 different integration schemes. Apart from this, however, in this work we restrict ourselves to a simple integration scheme based on  $m = 21$  integration directions defined on half of the unit-sphere according to Bažant and Oh (1986).

We can directly apply the algorithmic update scheme of the one-dimensional growth model described in Section 3 to the three-dimensional micro-sphere formulation. The discrete micro-sphere approach is based on a one-dimensional constitutive equation defined in terms of the (affine) stretch in every integration direction, i.e.,

$$\lambda^i = \sqrt{\mathbf{r}^i \cdot \mathbf{C} \cdot \mathbf{r}^i}. \quad (32)$$

We adopt the compressible neo-Hooke-type strain energy specified in Eq. (23). Note that different types of one-dimensional constitutive models can be chosen in the context of modelling biological tissues—for instance the worm-like chain model which provides a sound physical background and by means of the micro-sphere model can straightforwardly be extended to the three-dimensional case; see Kuhl et al. (2006), Alastrué et al. (2009), Menzel and Waffensch-

midt (2009) and references cited therein. Using Eqs. (28) and (29) together with the approximation (31), we can express the Piola–Kirchhoff stresses as

$$\mathbf{S} \approx \sum_{i=1}^m \left[ \frac{\rho_0^i}{\rho_0^*} \right]^{n^*} S^e w^i \mathbf{r}^i \otimes \mathbf{r}^i, \quad (33)$$

with  $S^e = \partial_{\lambda^i} \psi_0^e(\lambda^i) / \lambda^i$ , cf. Eq. (7).

In view of nonlinear finite-element simulations for example, we apply a Newton scheme to iteratively solve the global system of nonlinear equations. To ensure quadratic convergence of the algorithm, we compute the consistent algorithmic material tangent operator by the total differential of the Piola–Kirchhoff stresses  $\mathbf{S}$  with respect to the right Cauchy–Green deformation tensor  $\mathbf{C}$ , namely

$$\mathbf{E} = 2 \frac{d\mathbf{S}}{d\mathbf{C}} \approx 2 \sum_{i=1}^m \frac{d\mathbf{S}^i}{d\mathbf{C}} = \sum_{i=1}^m \mathbf{E}_\lambda^i + \mathbf{E}_{\rho_0}^i. \quad (34)$$

By means of the chain rule and by analogy to equations (16) and (17), we identify the two tangent contributions as

$$\mathbf{E}_\lambda^i = 2 \frac{\partial \mathbf{S}^i}{\partial \mathbf{C}} = 2 \frac{\partial \mathbf{S}^i}{\partial \lambda^i} \otimes \frac{\partial \lambda^i}{\partial \mathbf{C}} \quad \text{and} \quad \mathbf{E}_{\rho_0}^i = 2 \frac{\partial \mathbf{S}^i}{\partial \rho_0^i} \otimes \frac{\partial \rho_0^i}{\partial \mathbf{C}}, \quad (35)$$

which can be determined straightforwardly from the one-dimensional model, cf. Eq. (18) Table 2, as

$$\mathbf{E}_\lambda^i \approx \sum_{i=1}^m \frac{1}{[\lambda^i]^2} \left[ \frac{\rho_0^i}{\rho_0^*} \right]^{n^*} \bar{\mathbf{E}}_\lambda^i w^i \mathbf{r}^i \otimes \mathbf{r}^i \otimes \mathbf{r}^i \otimes \mathbf{r}^i \quad (36)$$

and

$$\mathbf{E}_{\rho_0}^i \approx \sum_{i=1}^m \frac{1}{[\lambda^i]^2} \left[ \frac{\rho_0^i}{\rho_0^*} \right]^{n^*} \bar{\mathbf{E}}_{\rho_0}^i w^i \mathbf{r}^i \otimes \mathbf{r}^i \otimes \mathbf{r}^i \otimes \mathbf{r}^i. \quad (37)$$

**Table 4**

Constitutive box for the three-dimensional micro-sphere-based density-growth model.

0. given deformation in terms of the right Cauchy-Green tensor  $\mathbf{C}$  at time  $t_{n+1}$  and history data  $\rho_{0m}^i$  of internal density variables at time  $t_n$  for all  $m$  discrete direction vectors  $\mathbf{r}^i \in \mathbb{U}^2$
1. compute affine micro-stretches for  $i = 1, \dots, m$

$$\lambda^i = \sqrt{\mathbf{r}^i \cdot \mathbf{C} \cdot \mathbf{r}^i}$$

2. evaluate step 1. and 2. of Table 2 using affine micro-stretches, i.e.,  $\lambda^i \equiv \lambda$ , for  $i = 1, \dots, m$
3. compute macroscopic Piola–Kirchhoff stresses

$$\mathbf{S} = \sum_{i=1}^m \frac{1}{\lambda^i} \left[ \frac{\rho_0^i}{\rho_0^*} \right]^{n^*} \frac{\partial \psi_0^e}{\partial \lambda^i} \mathbf{w}^i \mathbf{r}^i \otimes \mathbf{r}^i$$

4. compute tangent operator

$$\mathbf{E} = \sum_{i=1}^m \frac{1}{[\lambda^i]^2} \left[ \frac{\rho_0^i}{\rho_0^*} \right]^{n^*} \left[ \bar{\mathbf{E}}_\lambda^i + \bar{\mathbf{E}}_{\rho_0}^i \right] \mathbf{w}^i \mathbf{r}^i \otimes \mathbf{r}^i \otimes \mathbf{r}^i \otimes \mathbf{r}^i$$

wherein  $\bar{\mathbf{E}}_\lambda^i$  and  $\bar{\mathbf{E}}_{\rho_0}^i$  are taken from Table 2

5. compute zeroth-, second-, and fourth-order density moments  $A$ ,  $\mathbf{A}$  and  $\mathbf{A}$  for visualisation purposes, cf. A.2

The algorithm related to the constitutive micro-sphere model is summarised in Table 4.

#### 4.3. Numerical example

As an illustrative numerical example to emphasise the properties of the computational anisotropic growth model, we next discuss a homogeneous state of three-dimensional deformation. We use the neo-Hookean strain energy function specified in Section 3 together with the material parameters summarised in Table 3. The time step size  $\Delta t$  is set to 1.0 [d] and the Newton-tolerance is  $\text{tol} = 10^{-8}$ . We apply stepwise loading by prescribing external tensile and compressive forces, namely  $\mathbf{F}_1 = F_{\text{tens}} \mathbf{e}_1$  and  $\mathbf{F}_2 = F_{\text{comp}} \mathbf{e}_2$  with  $F_{\text{tens}} = -2F_{\text{comp}}$ . The specific loading history is displayed in Fig. 4(a). Here and as this work proceeds, we make use of a Cartesian frame  $\{\mathbf{e}_1, \mathbf{e}_2, \mathbf{e}_3\}$ , respectively  $\{\mathbf{e}_x, \mathbf{e}_y, \mathbf{e}_z\}$ .

Due to the application of the algorithmic micro-sphere scheme, we obtain  $m$  different micro-densities  $\rho_0^i$ . In this regard, making use of the stereographic pole projection method seems to be the most feasible approach to visualise the micro-densities  $\rho_0^i$  directly, cf. A.1. As a scalar measure representing the macroscopic density we introduce a density moment of zeroth-order denoted by  $A$ , cf. A.2. Fig. 4(b) illustrates the evolution of this density-related quantity  $A$ . As expected from the response of the one-dimensional model, we observe a characteristic creep-type behaviour saturating in a time-dependent manner towards the biological equilibrium state.

As we will further discuss in the following, material anisotropy evolves for the present model proposed so that the importance and influence of the accuracy of the integration scheme is less pronounced as for the case of non-evolving material anisotropy; see also Menzel and Waffenschmidt (2009) and Alastrué et al. (2009). Nevertheless, we perform a sensitivity analysis to study the impact of the number of integration directions for a homogeneous deformation. For the deformation considered, it turns out that the  $m = 21$ -point integration scheme yields results comparable to those obtained by in general more accurate higher-order integration schemes; see also Miehe et al. (2004), Alastrué et al. (2009) or Ehret et al. (2010) for more detailed discussion on the influences of the numerical integration schemes over the unit-sphere. In this contribution we take into account three integration schemes reported in Bažant and Oh (1986) and 14 integration

schemes provided in Heo and Xu (2001) where we consider the integration scheme of highest order with  $m = 600$  integration directions per hemisphere as a reference solution. For the sake of clarity only four different integration schemes with  $m = \{21, 37, 146, 600\}$  are compared in Fig. 4(c). We observe that the  $m = 21$ -point integration scheme shows good agreement with the reference solution, whereas the  $m = 146$ -point and especially the  $m = 37$ -point integration schemes show significant deviations compared to the  $m = 600$ -reference. More significantly, we evaluate the zeroth-order moment  $A$  at  $t = 800$  [d] in Fig. 4(c) and compare 16 different integration schemes to the  $m = 600$ -solution which is additionally illustrated by a horizontal reference line. Generally, we observe that a higher number of integration directions does not necessarily lead to more accurate results with respect to the chosen reference solution. Interestingly, the lower-order integration schemes, as, e.g., the  $m = 21$ - and especially the  $m = 33$ - and  $m = 78$ -point integration schemes show excellent agreement with the reference solution for the considered deformation. We will make use of the  $m = 21$ -point integration scheme for all subsequent simulations.

In order to further study the anisotropic evolution of the density, we make use of different visualisation techniques which are discussed in more detail in A. The application of the micro-sphere scheme offers several beneficial possibilities to illustrate local anisotropic behaviour. We make use of stereographic pole projection plots, cf. A.1, and orientation-distribution-type surface plots, cf. A.2, which we evaluate at five different points in time, namely  $t = \{0, 200, 400, 600, 800\}$  [d].

The stereographic pole projection plots in Fig. 5(a) show the evolution of the individual micro-densities  $\rho_0^i$  with the  $z$ -direction being perpendicular to the projection plane. The initial isotropic state at  $t = 0$  (blue<sup>1</sup>) corresponds to  $\rho_0^i = \rho_0^* = 1.0 \forall i = 1, \dots, m$ . With progressing deformation, the density distribution changes significantly, resulting in a densification (red) in the main loading directions and a resorption (dark blue) in the unloaded directions. This clearly reflects a direction-dependent or rather anisotropic growth process including texture evolution.

In addition, we visualise the anisotropic density evolution by means of orientation-distribution-function-related quantities in Fig. 5(b, c), where Fig. 5(b) displays the second-order density moment  $\mathbf{A}$ , which takes the representation of generalising the two-dimensional orientation-distribution-function-type plots by Jacobs et al. (1997) to the three-dimensional case. Fig. 5(c) shows the fourth-order density moment  $\mathbf{A}$ , see also A.2. In both cases, the initial isotropic state (blue) is characterised by a sphere with radius 1.0 since the initial micro-densities  $\rho_0^i = \rho_0^* = 1.0 \forall i = 1, \dots, m$ . With increasing deformation the shape and the size of the orientation-distribution-function-related quantities change significantly. The shape of these higher-order density-related functions characterises the anisotropy evolution while their size represents the growth process itself.

#### 5. Finite element modelling of anisotropic growth

This section covers an application example of the anisotropic density growth formulation as outlined in the previous sections and particularly deals with the simulation of a proximal tibia bone under physiological loading conditions and a comparison to experimental measurements. We refer to Kuhl et al. (2003) for a detailed discussion on aspects of finite element implementation, whereas in a recent publication by Pang et al. (2012) the same tibia bone structure is investigated in response to gait.

<sup>1</sup> For interpretation of colour in figures, the reader is referred to the Web version of this article.

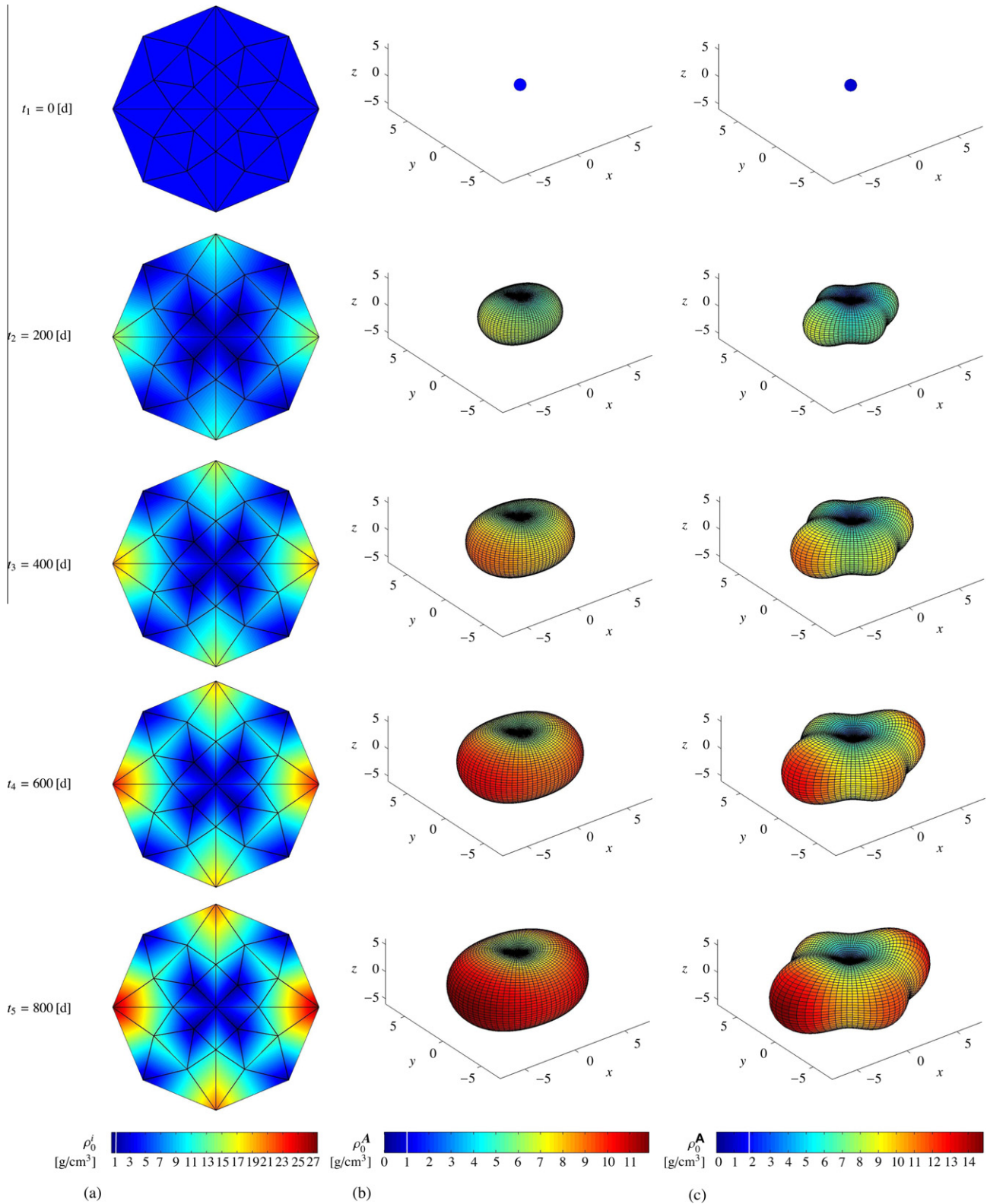


**Fig. 5.** Visualisation of anisotropic density evolution with respect to five representative points in time  $t_1, \dots, t_5$ . (a) Stereographic pole projection plots visualising the microdensities  $\rho_0^j$  and orientation distribution-type surface plots (b) based on second-order density moment  $\mathbf{A}$  and (c) based on fourth-order density moment  $\mathbf{A}$ . Density-related values larger than one characterise densification whereas values smaller than one represent resorption;  $\rho_0 = 1.0 \text{ [g/cm}^3\text{]}$ .

**5.1. Subject-specific problem—proximal tibia**

We now apply the proposed anisotropic growth model to a subject-specific three-dimensional part of a proximal tibia. The three-dimensional tibia model consists of 3190 linear displacements

ment-based tetrahedral finite elements and 893 nodes, see Fig. 6(a). The respective densities  $\rho_0^j$  are stored as internal variables at the finite element integration point level.

We specify the geometry and boundary conditions according to Pang et al. (2012), where bone density profiles of a proximal tibia

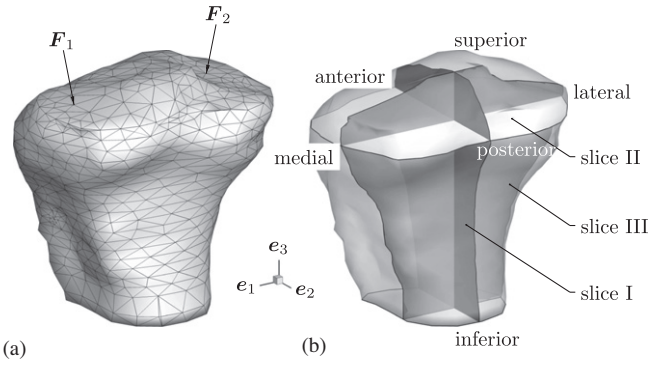


**Fig. 6.** Geometry of the upper part of the proximal tibia. (a) Finite element mesh with applied concentrated forces  $F_1, F_2$  and (b) location of slices I (sagittal slice), II (axial slice) and III (coronal slice) used in Figs. 9–13.

have been studied in response to gait. With regard to the applied Dirichlet boundary conditions, we clamp the displacements at one single node at the bottom of the specimen, i.e.,  $\mathbf{u} = \mathbf{x} - \mathbf{X} = \mathbf{0}$ , whereas all other displacements at the bottom nodes are constrained solely in  $\mathbf{e}_2$ - and  $\mathbf{e}_3$ -direction, i.e.,  $\mathbf{u} \cdot \mathbf{e}_2 = \mathbf{u} \cdot \mathbf{e}_3 = 0$ . Furthermore, we apply Neumann boundary conditions by prescribing two concentrated forces at two nodes at the top of the specimen, as schematically drawn in Fig. 6(a). To be specific,  $\mathbf{F}_1 = 25.4545\mathbf{e}_1 - 305.4545\mathbf{e}_3$  [N] and  $\mathbf{F}_2 = -25.4545\mathbf{e}_1 - 254.5455\mathbf{e}_3$  [N]; cf. Pang et al. (2012). We apply these external forces by linearly increasing their magnitude within 5.0 [d] and keep  $\mathbf{F}_1$  and  $\mathbf{F}_2$  constant thereafter for 35.0 [d]. In view of the material parameters, we adopt the values summarised in Table 3 and the constant time step size of the calculations is  $\Delta t = 0.5$  [d].

To analyse the growth process in the proximal tibia under the prescribed loading conditions, we display the evolution of the zeroth-order density moment  $A$  at four different points in time,  $t = \{10, 20, 30, 40\}$  [d], cf. Fig. 7. After 10 [d]—the external forces possessing their final maximum magnitudes already after 5 [d]—we observe a remarkable densification of the tibia, in particular in those regions of the bone which are predominantly affected by the loading and in consequence associated with high levels of strain energy. However, during the subsequent part of the time period considered, the accumulated density does not change significantly in these areas. Instead, as time progresses, the material located at rather non-weight bearing regions—associated with lower strain energy levels—tends to degrade until the biological equilibrium state is reached. At biological equilibrium, the material—as represented by its local densities—is distributed such that the bone provides optimal structural support for forces induced during gait, cf. Pang et al. (2012).

Since the growth process, as modelled in this contribution, is anisotropic, it is reasonable to investigate the evolution of anisotropy by means of representative anisotropy measures. As a scalar-valued quantity we use the difference in maximum and minimum principal values of the second-order density moment,  $A_1 - A_3$ , see A.2. This anisotropy measure is depicted as a contour plot in Fig. 8 and referred to four different points in time. The initial isotropic state at  $t = 0$  (blue) corresponds to  $A_1 - A_3 = 0$ . It is clearly seen that the degree of anisotropy changes most significantly in those regions which are predominantly associated with the loading and thus with a high strain energy level. Interestingly, even if the outer upper part of the tibia does not contribute much to the support of the loading, and in consequence degenerates with time, the degree of anisotropy also rises in these regions as time progresses.

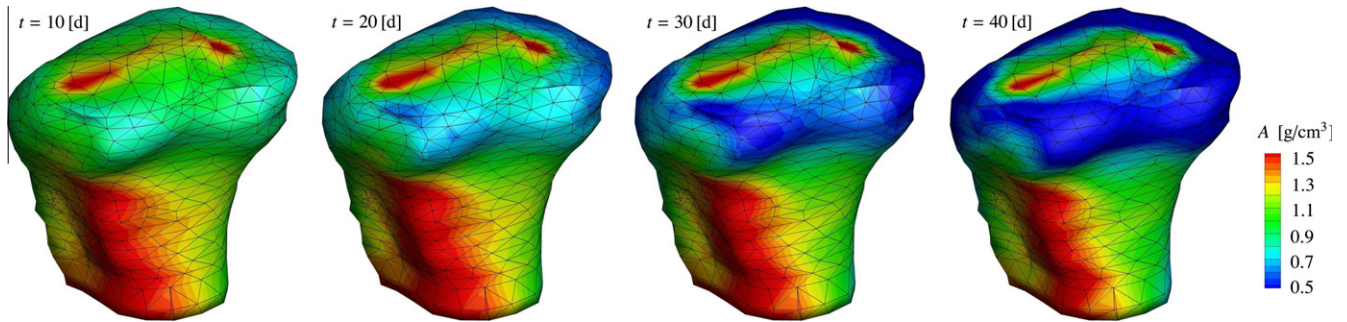


**Fig. 7.** Three-dimensional density evolution in the proximal tibia at four different points in time,  $t = \{10, 20, 30, 40\}$  [d]. The colour code indicates the evolution of the bone density by means of visualising the zeroth order moment  $A$ . As time progresses, from left to right, the bone densifies in areas of high strain energy and degrades in areas of low strain energy until it has approached the biological equilibrium at  $t = 40$  [d].

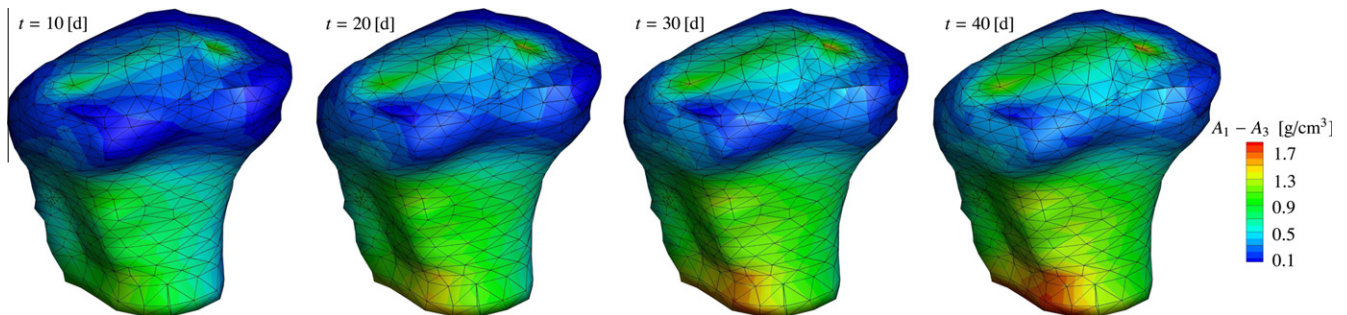


**Fig. 8.** Three-dimensional anisotropy evolution in the proximal tibia at four different points in time,  $t = \{10, 20, 30, 40\}$  [d]. The colour code indicates the evolution of the anisotropy by means of visualising the difference between the maximum and minimum principal value of  $A$ , i.e.,  $A_1 - A_3$ . As time progresses, from left to right, the anisotropy evolves most significantly in those regions which are predominantly associated with the loading and thus with a high strain energy level.

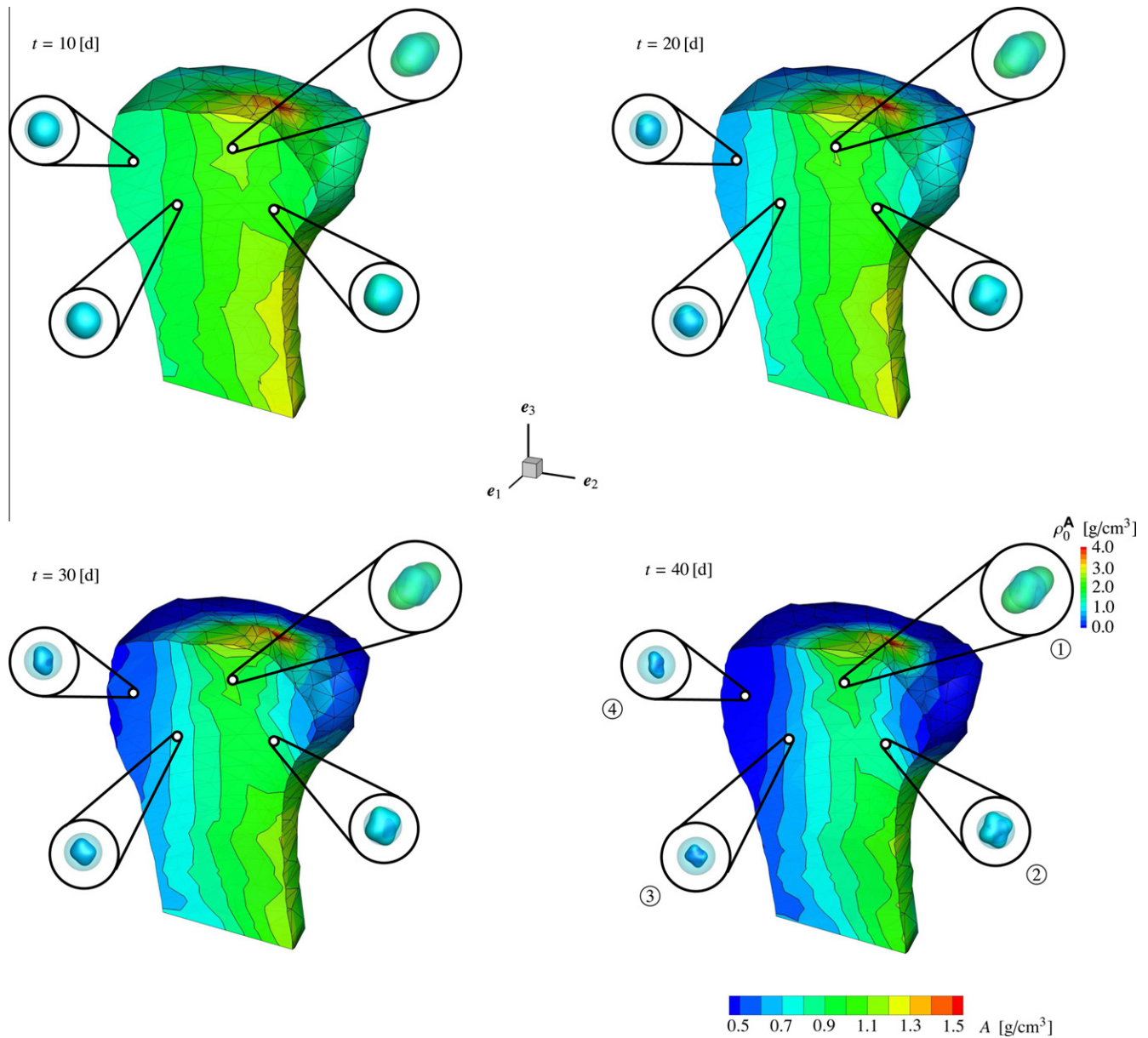


**Fig. 9.** Anisotropy evolution in the proximal tibia displayed at four representative integration points located (approximately) in slice I, cf. Fig. 6(b), and visualised by means of odfs based on fourth-order density moments  $\mathbf{A}$ , whereby the isotropic initial state is plotted additionally as a reference state (shaded sphere). A change in size of the odf is attributed to densification/resorption; a change in shape of the odf is attributed to a change of anisotropic material properties. The colour code used for the bone indicates the evolution of the bone density by means of visualising the zeroth-order density moment  $A$ .

To investigate the evolution of anisotropy and density in more detail, we now focus on three cross sections or rather slices of the tibia. The first slice I is placed parallel to the  $e_2$ - $e_3$  plane and the second slice II is oriented parallel to the  $e_1$ - $e_2$  plane, whereas slice III is perpendicular to  $e_2$ ; see Fig. 6(b). Within the first two slices, four integration points of particular finite elements are chosen in order to visualise local anisotropic material properties by means of the fourth-order moment  $\mathbf{A}$  or rather its corresponding orientation distribution function (odf)  $\rho_0^{\mathbf{A}}$ ; see Eq. (A.12). We also make use of the fourth-order compliance tensor  $\mathbf{C}^e$  to represent directional Young's modulus surface plots which are based on the odf  $\delta^{-1}\mathbf{C}^e$ ; see Eq. (A.14) and Fig. A.15(e-f) for the visualisation of three different types of material symmetry.

Fig. 9 shows the local evolution of anisotropy with respect to time at four different integration points located within slice I. As expected, we observe that odf ①—located at the top of the bone

close to where the load is applied—shows the most significant change in size and shape, which reflects a pronounced growth behaviour accompanied by a considerable change of anisotropic material properties. The other odfs ②–④ also show anisotropic behaviour or rather texture evolution, since their shape increasingly deviates from their initial spherical distribution, which, here and in the following, is indicated by the superimposed transparent sphere. In contrast to odf ①, however, the odfs ②–④ shrink which clearly indicates the resorption process of the material located in these points.

By analogy to the considerations above, Fig. 10 illustrates the local evolution of anisotropy at four other integration points, now located within slice II. In this case, we observe that especially odf ⑦ shows a very pronounced and elongated shape in combination with a drastic change in size. The distribution of this odf corresponds to an almost transversely isotropic state. At  $t = 10$  [d],

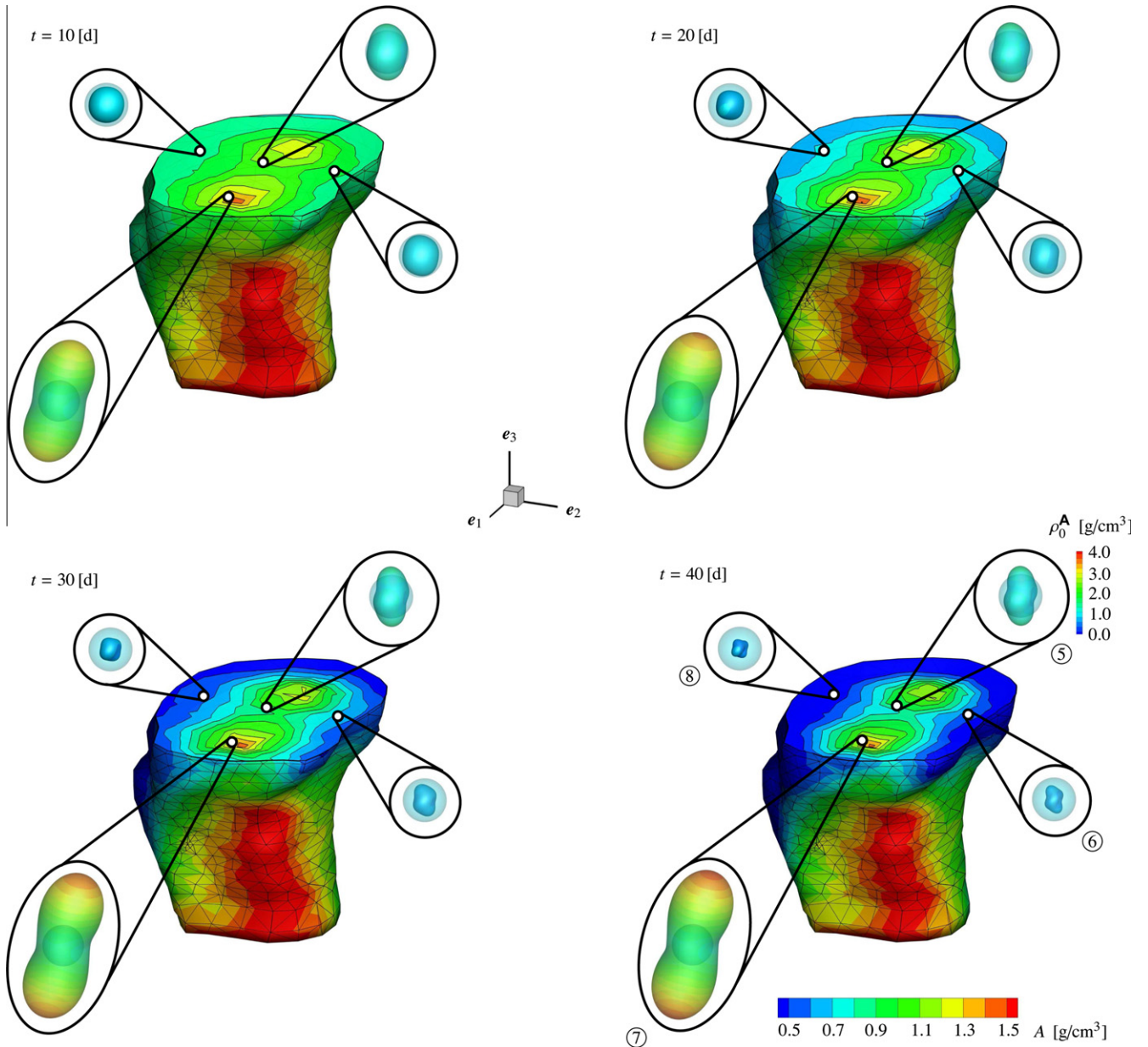


**Fig. 10.** Anisotropy evolution in the proximal tibia displayed at four representative integration points located (approximately) in slice II, cf. Fig. 6(b), and visualised by means of odfs based on fourth-order density moments  $\mathbf{A}$ , whereby the isotropic initial state is plotted additionally as a reference state (shaded sphere). A change in size of the odf is attributed to densification/resorption; a change in shape of the odf is attributed to a change of anisotropic material properties. The colour code used for the bone indicates the evolution of the bone density by means of visualising the zeroth-order moment  $A$ .

when the other odfs do not show any pronounced changes, odf ⑦ has almost reached its final state. This effect results from the point, to which odf ⑦ is referred to, being located in the region close to where the external force  $\mathbf{F}_1$  is applied. The concentric isolines in the contour plots within slice I show these load bearing regions.

To investigate the evolution of the elastic or rather stiffness properties of bone, we additionally make use of Young's modulus surface plots evaluated within the same slices and at the same integration points as introduced and used above. The density-power-weighted elasticity tensor  $\mathbf{E}_\lambda$  in the unloaded initial state at  $t = 0$  [d] can be calculated from Eqs. (36) and (A.6). For the specific case of the neo-Hooke-type strain energy and by using Eqs. (24) and (25) we obtain

$$\mathbf{E}_\lambda|_{t=0[d]} = \frac{1}{3} [\lambda^* + 2\mu^*] \left[ \mathbf{I}^{\text{vol}} + \frac{2}{5} \mathbf{I}^{\text{dev}} \right], \quad (38)$$

wherein  $\mathbf{I}^{\text{vol}} = \frac{1}{3} \mathbf{I} \otimes \mathbf{I}$  and  $\mathbf{I}^{\text{dev}} = \mathbf{I}^{\text{sym}} - \mathbf{I}^{\text{vol}}$  denote the fourth-order volumetric and deviatoric identity tensors with  $\mathbf{I}$  and  $\mathbf{I}^{\text{sym}} = \frac{1}{2} [\mathbf{I} \otimes \mathbf{I} + \mathbf{I} \otimes \mathbf{I}]$  representing the second- and fourth-order symmetric identity tensors. Eq. (38) reflects an initially isotropic, i.e., spherical, distribution of the Young's modulus surface plot with a value of  $\delta^{-1c^e} = 850.33 \text{ [N/mm}^2] \forall \mathbf{r}$ ; cf. Figs. 11 and 12 where the isotropic reference state is visualised as a shaded sphere. Note that the micro-sphere-based tensor  $\mathbf{E}_\lambda|_{t=0[d]}$  does not coincide with the initial elasticity tensor obtained from a standard isotropic neo-Hookean continuum model—in particular the material parameters  $\lambda^*$  and  $\mu^*$  do not weight different modes but the sum  $\lambda^* + 2\mu^*$  scales both, the volumetric and deviatoric modes. Fig. 10 shows the local state of anisotropy, now visualised by means of Young's modulus surface plots, at the four different integration points located within slice I. As expected from the previous observations, odf ①—located at the top of the bone close to the loading point—shows the most

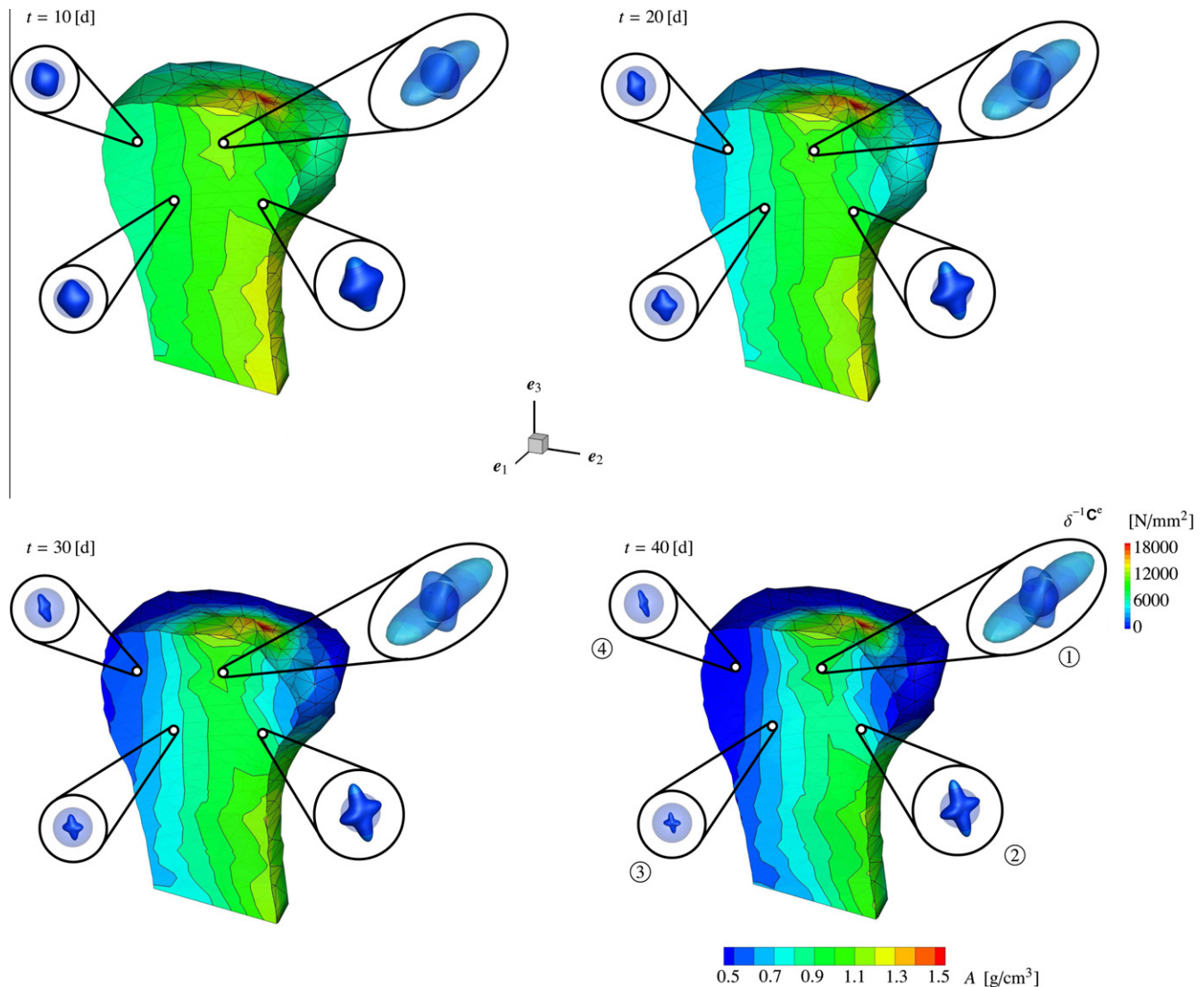


**Fig. 11.** Anisotropy evolution in the proximal tibia displayed at four representative integration points located (approximately) in slice I, cf. Fig. 6(b), and visualised by means of Young's modulus surface plots, whereby the isotropic initial state is plotted additionally as a reference state (shaded sphere). A change in size of the odf is attributed to densification/resorption; a change in shape of the odf is attributed to a change of anisotropic material properties. The colour code used for the bone indicates the evolution of the bone density by means of visualising the zeroth-order density moment  $A$ .

significant increase in size and change in shape, which reflects a pronounced growth and remodelling behaviour accompanied by a considerable evolution of anisotropic material properties. To give an example, the maximum value of the directional Young's modulus for odf ① is 4048 [N/mm<sup>2</sup>]. The other odfs ②–④ also show evolution of material anisotropy but accompanied by a shrinkage in size indicating the resorption process of the material taking place at these material points. For all four integration points, we can identify pronounced orthotropic material properties; see also Fig. A.15(f). By analogy to the considerations above, Fig. 12 illustrates the local state of anisotropy at the four integration points located within slice II. Similar to odf ⑦ for  $\rho_0^A$  in Fig. 11, to odf ⑦ for  $\delta^{-1}C^e$  in Fig. 12 possesses a very pronounced and elongated shape in combination with a drastic change in size—note the different scaling factors or rather diameters of the respective initial spherical odfs. The distribution ⑦ corresponds to an almost transversely isotropic state, whereas the other odfs again exhibit orthotropic behaviour. The maximum value of the directional Young's modulus for odf ⑦ is 17300 [N/mm<sup>2</sup>]. Experiments reported in the literature for the stiffness properties of the proximal tibia provides data within a range from 20 to 20000 [N/mm<sup>2</sup>]; see, e.g., the contribution by Williams and Lewis

(1982), the study by Goldstein (1987) for an extensive summary of data with respect to the anatomic location and function of bone in general and Ashman et al. (1989) for the tibial cancellous bone specifically, as well as Rho et al. (1998) for a literature survey of methods for determining the elastic modulus of trabecular bone.

To quantitatively compare our simulation with experimental results, we consider specific stiffness values obtained from the Young's modulus surface plots in Fig. 11 and compare these to respective stiffness values provided in the experimental study by Ashman et al. (1989). To give a brief summary, Ashman et al. (1989) investigated the anatomical variation of orthotropic elastic moduli of the cancellous bone from three human proximal tibiae using an ultrasonic technique. They found that the material properties are highly heterogeneous, with the axial modulus ranging between 340 [N/mm<sup>2</sup>] and 3350 [N/mm<sup>2</sup>]*—*in other words, the measured Young's moduli depend on the anatomical position. Moreover, the authors showed that the degree of anisotropy of the cancellous bone, determined by the relative differences between three orthogonal moduli, turned out to be more homogeneous than the respective distributions of the Young's moduli themselves. Table 5 provides extremal values of directional

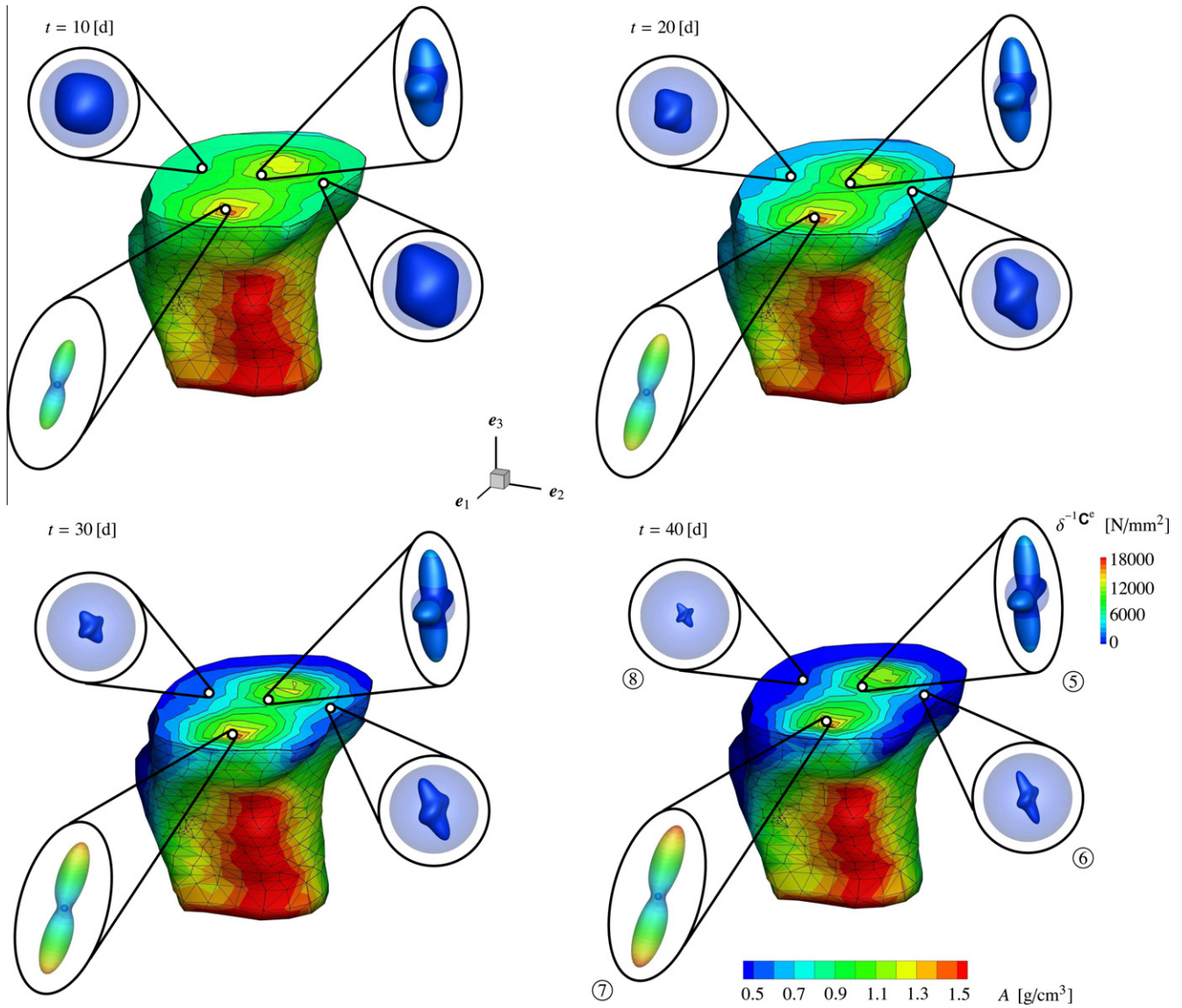


**Fig. 12.** Anisotropy evolution in the proximal tibia displayed at four representative integration points located (approximately) in slice II, cf. Fig. 6(b), and visualised by means of Young's modulus surface plots, whereby the isotropic initial state is plotted additionally as a reference state (shaded sphere, note the different scaling). A change in size of the odf is attributed to densification/resorption; a change in shape of the odf is attributed to a change of anisotropic material properties. The colour code used for the bone indicates the evolution of the bone density by means of visualising the zeroth-order moment  $A$ .

Young's moduli  $E_{i'}$ , with the index  $i' = 1, 2, 3$  being referred to the related principal directions. For the present study, these are almost aligned with the base system  $e_i$ , with  $i = 1, 2, 3$ , as highlighted in Fig. 12. Consequently  $E_{1'}$  corresponds approximately to the lateral-medial axis,  $E_{2'}$  is related to the anterior-posterior axis, and  $E_{3'}$  can be referred to the inferior-superior axis. These extremal values are based on the odfs for  $\delta^{-1}C^e$  at the four integrations points ⑤–⑧ located in slice II which are specified and visualised in Fig. 12. When comparing the simulation results for  $E_{i'}$  with the three orthogonal Young's moduli  $E_j$  reported in Ashman et al. (1989), we have to notice that  $E_j$  are not referred to exactly the same axes as the directional Young's moduli  $E_{i'}$  considered in this work. Furthermore,  $E_1$  is referred to the anterior-posterior axis and  $E_2$  reflects the material properties along the lateral-medial axis. Nevertheless, the values for the directional Young's moduli as summarised in Table 5 together with their relative differences characterising the respective degree of anisotropy, are within the same range as those identified by Ashman et al. (1989). Odf ⑦ deviates from the experimental results as the simulation predicts, in con-

**Table 5**

Extremal values of directional Young's moduli  $E_{i'}$  in  $[N/mm^2]$ , for  $i' = 1, 2, 3$ , and relative differences for each odf, which characterise the respective degree of anisotropy, as given in Fig. 12.

Odf	$E_{1'}$	$E_{2'}$	$E_{3'}$	$\frac{E_{2'} - E_{1'}}{E_{1'}}$	$\frac{E_{3'} - E_{1'}}{E_{1'}}$	$\frac{E_{2'} - E_{3'}}{E_{3'}}$
⑤	1600	300	2300	-81%	-86%	-30%
⑥	300	60	550	-80%	-89%	-45%
⑦	1400	4000	17300	186%	-77%	-92%
⑧	280	50	250	-82%	-80%	12%

trast to the other odfs discussed, a transversely isotropic distribution. Furthermore, apart from odf ⑦, the relative differences between  $E_{2'}$  and  $E_{1'}$ , respectively  $E_{2'}$  and  $E_{3'}$ , are nearly constant, even though the respective densities and directional Young's moduli are rather different. This property is in agreement with the observations made in Ashman et al. (1989), i.e., the degree of anisotropy is almost constant within a large range of cancellous bone densities. Note that the averaged values of relative differ-

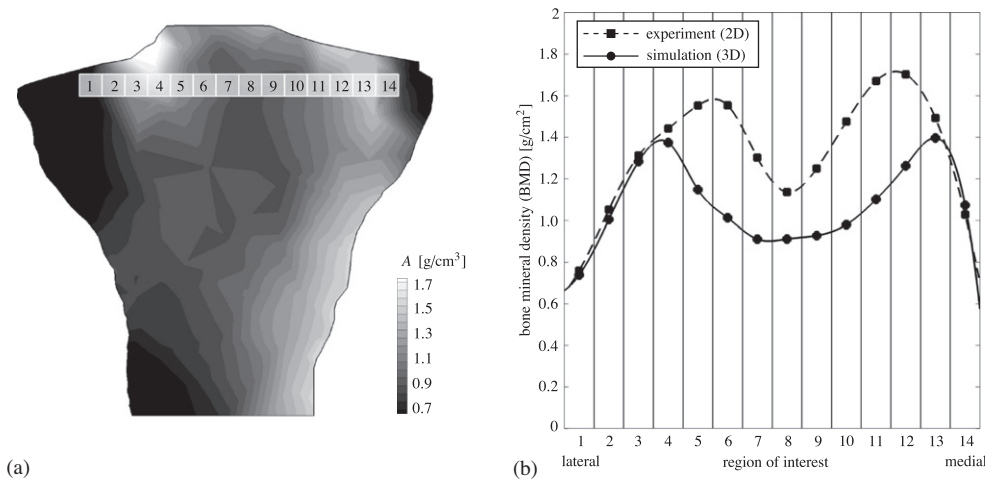


**Fig. 13.** Region of interest method to characterise regional density variations in the proximal tibia. (a) The local bone mineral density (BMD) is evaluated in fourteen equal-sized regions along the width of tibial slice III, cf. Fig. 6(b). (b) Regional variation of bone mineral density in fourteen regions of interest. Squares and dotted lines indicate the experimentally measured bone mineral density extracted from the Dual-Energy X-ray Absorptiometry scan as reported in Pang et al. (2012). Circles and solid lines indicate the computationally predicted bone density extracted from the three-dimensional simulation.

ences in orthogonal Young's moduli reported in Ashman et al. (1989) are based on three proximal human tibiae using 25 cancellous portions of each specimen. These also stem from different axial cross-sections, whereas we merely consider data at four chosen locations in one axial slice. Moreover, Ashman et al. (1989) investigated a different specimen than the one discretised in this work.

### 5.2. Three-dimensional density prediction

To quantitatively verify our three-dimensional simulations of the tibia, we adopt the region of interest method—analogue to Pang et al. (2012) and described in, e.g., Hulet et al. (2002)—and evaluate the local bone mineral density (BMD) in fourteen equal-sized regions along the width of a characteristic tibial cross section. In particular, we consider slice III, see Fig. 6(b), to which we apply a grey-scaled contour plot of the zeroth-order moment  $A$  representing the macroscopic density distribution as illustrated in Fig. 13(a). Based on this, a computationally predicted bone mineral density profile is calculated from grey-scaled bone density profiles by averaging the density values of 2500 pixels within each region of interest and plotted over the width of the slice using a cubic spline data interpolation; see Fig. 12(b). We compare this computationally predicted BMD-profile to an experimentally measured subject-specific local bone mineral density profile, which was recorded by a Dual-Energy X-ray Absorptiometry (DEXA) scan as reported in Pang et al. (2012). The resulting regional variations of the bone mineral density in the fourteen regions of interest are summarised and compared in Fig. 12(b). Especially in the lateral regions 1–4 and 13, 14 we observe a good qualitative and quantitative agreement between experimental data and simulation results. Larger deviations are observed in the inner regions where the values of the bone mineral density are underestimated. This is illustrated by an inner region of lower density values in regions 5–12 between the two peak values.

### 5.3. Potential limitations

The observed discrepancies between computationally simulated and experimentally measured BMD-profiles, as shown in the previous subsection, can on the one hand be attributed to the lack of representative experimental data to compare the simulation with. On the other hand, the misfit can also be explained by

the following specific properties of the model and discrete boundary value problem considered, see also Pang et al. (2012).

#### 5.3.1. Geometry and mesh

The three-dimensional mesh representing the proximal tibia is a generic mesh *not* created based on the subject's own geometry from which the BMD-profile is extracted. As a consequence, neither the chosen cross-section of the tibia, slice III, nor the region of interest might be fully representative for a comparison with the two-dimensional DEXA scan. In this regard, it is also worth to note that DEXA calculates the BMD using *area* measures, instead of providing mass divided by *volume*. In addition, the mesh itself is relatively coarse, especially in the middle region where we observe larger differences between experimentally measured and computationally simulated densities.

#### 5.3.2. Material parameters

We assume the same material parameters as calibrated in Pang et al. (2012). However, since we apply a different material model—the micro-sphere-based neo-Hookean-type model can not be reduced to the macroscopic continuum neo-Hookean model—the material parameters also take a different interpretation. Furthermore, we assume that the bone possesses initially homogeneous and isotropic material properties. However, as also stated in Pang et al. (2012), the material properties of the collagen matrix in the subchondral bone are far from being uniform or isotropic in a state which we adopt as the initial configuration. In reality, the outer layer of the tibia consists of cortical bone with a higher density, which does not change in time, while the inner part is composed of the less dense trabecular bone.

#### 5.3.3. Boundary conditions

As also discussed in Pang et al. (2012), we have simplified the tibiofemoral loading by two representative concentrated forces acting on a single medial and lateral node each. In reality, however, the articular cartilage interface between the femur and tibia can be strained, the representative loading can shift in space and, most importantly, is spread over an area. Furthermore, we neglect forces from muscles, tendons, and the tibiofemoral joint. Lastly, we assume the subchondral bone to be completely isolated, whereas in reality a contact region with the proximal fibula affects the in vivo loading situation through an elastic interface.

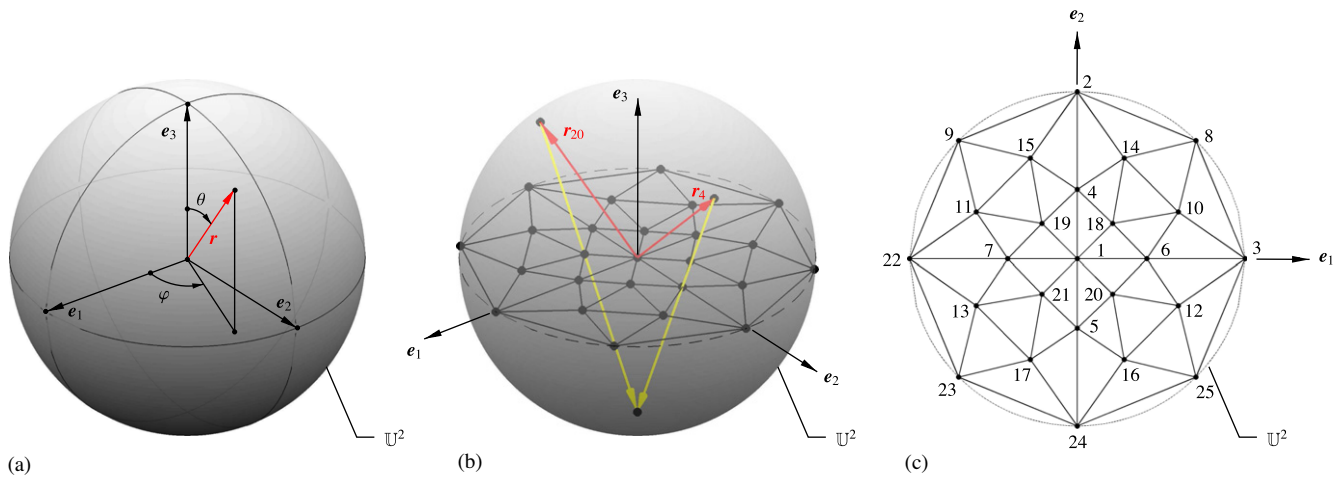


**Fig. A.14.** Stereographic projection: (a) Unit vector  $\mathbf{r}$  parameterised by spherical angles  $\varphi$  and  $\theta$  with a Cartesian base system  $\mathbf{e}_1, \mathbf{e}_2, \mathbf{e}_3$ ; (b) Graphical illustration of the method of stereographic projection for  $m = 21$  integration directions (in the upper half-sphere) by means of two exemplary unit vectors  $\mathbf{r}_4$  and  $\mathbf{r}_{20}$ ; (c) Two-dimensional pole projection plot. Points 22–25 are added for visualisation purpose, cf. Miehe et al. (2004).

Apart from these purely mechanical limitations, other equally important aspects like, e.g., biochemical factors, age, gender, race, or family history are not taken into account.

## 6. Summary

Bones adapt their local density and load bearing capacities to mechanical stimuli. Densification of the bone in mechanically high load-bearing regions as well as resorption in region with a low load is observed. This adaptation results in texture evolution and highly anisotropic material properties of the bone.

To model and simulate such anisotropic growth phenomena in bone, we propose a micro-sphere model which allows to straightforwardly extend one-dimensional constitutive models to an anisotropic three-dimensional formulation. We adopt a well-established one-dimensional model, previously used in the context of three-dimensional but isotropic growth, which includes energy-driven evolution of directional densities. These directional densities are referred to the integration direction of the micro-sphere and, as an advantage of the model developed, enable to compute higher-order tensorial density moments. By analogy to so-called Young's moduli plots common in the context of modelling and simulation texture phenomena, the visualisation of such higher-order density moments provides detailed insights into the simulated deformation-induced anisotropic local material properties. Apart from discussing the micro-sphere-based anisotropic growth model under homogeneous deformations, we investigate the finite element simulation of anisotropic growth in proximal tibia bone. The simulation results capture the densification effects and clearly identify the main load bearing regions. Local anisotropy evolution is visualised by means orientation-distribution-function-type representations of higher-order density moments.

At this stage, the simulation results of macroscopic density distributions are in reasonable agreement with experimental investigations reported in Pang et al. (2012). In the future, the comparison of simulated local anisotropic material properties with related experimental data will be of high interest. The incorporation of deformation-induced anisotropic adaptation and texture evolution is also of key relevance in view of the modelling and simulation of the interaction of bones with implants as discussed by García et al. (2002) and Moreo et al. (2007). Growth phenomena in biological tissues in general effect both changes in density or rather mass and changes in volume. One modelling approach to include

changes in volume is the so-called multiplicative decomposition of the deformation gradient; see Taber (1995) and Kuhl et al. (2007) with application of an isotropic multiplicative growth model to the finite-element-simulation of an artery. Such growth models are also developed for anisotropic tissues, see Lubarda and Hoger (2002), and embedded into iterative finite element formulations to simulate complex boundary value problems; see Menzel (2006), Menzel (2007) and Göktepe et al. (2010). In the future, the anisotropic micro-sphere model can be combined with the kinematics of multiplicative growth so that additional changes in volume are directly addressed within the constitutive model; see Harrysson et al. (2010) where a micro-sphere model is combined with a multiplicative decomposition of the deformation gradient to simulate the deformation-induced anisotropy evolution in glassy polymers.

## Acknowledgements

Parts of this work were supported by the National Science Foundation CAREER award CMMI-0952021 and the National Institutes of Health Grant U54 GM072970 to Ellen Kuhl.

## Appendix A. Visualisation of anisotropy

The Appendix addresses different techniques used in this paper to visualise anisotropic material properties. To be specific, we make use of stereographic pole projection plots, A.1, as applied in, for example, Miehe et al. (2004) and Alastrué et al. (2009). Additionally, we apply two different kinds of orientation-distribution-type surface plots which we discuss in A.2. Here, we refer to Hashash et al. (2003) and Kriz et al. (1995) for detailed reviews on visualising higher-order tensors and to Menzel et al. (2008) and Menzel and Waffenschmidt (2009), where similar representations have been utilised in the context of fibrous soft biological tissue. A general overview on visualisation techniques for anisotropic material properties and texture evolution is provided in Kocks et al. (2000) and references cited therein.

### A.1. Stereographic pole projection

By means of the method of stereographic projection, we project scalar quantities—in the present context the micro-densities  $\rho_0^i$ —related to the vectorial integration directions  $\mathbf{r}^i \in \mathbb{U}^2$  onto the

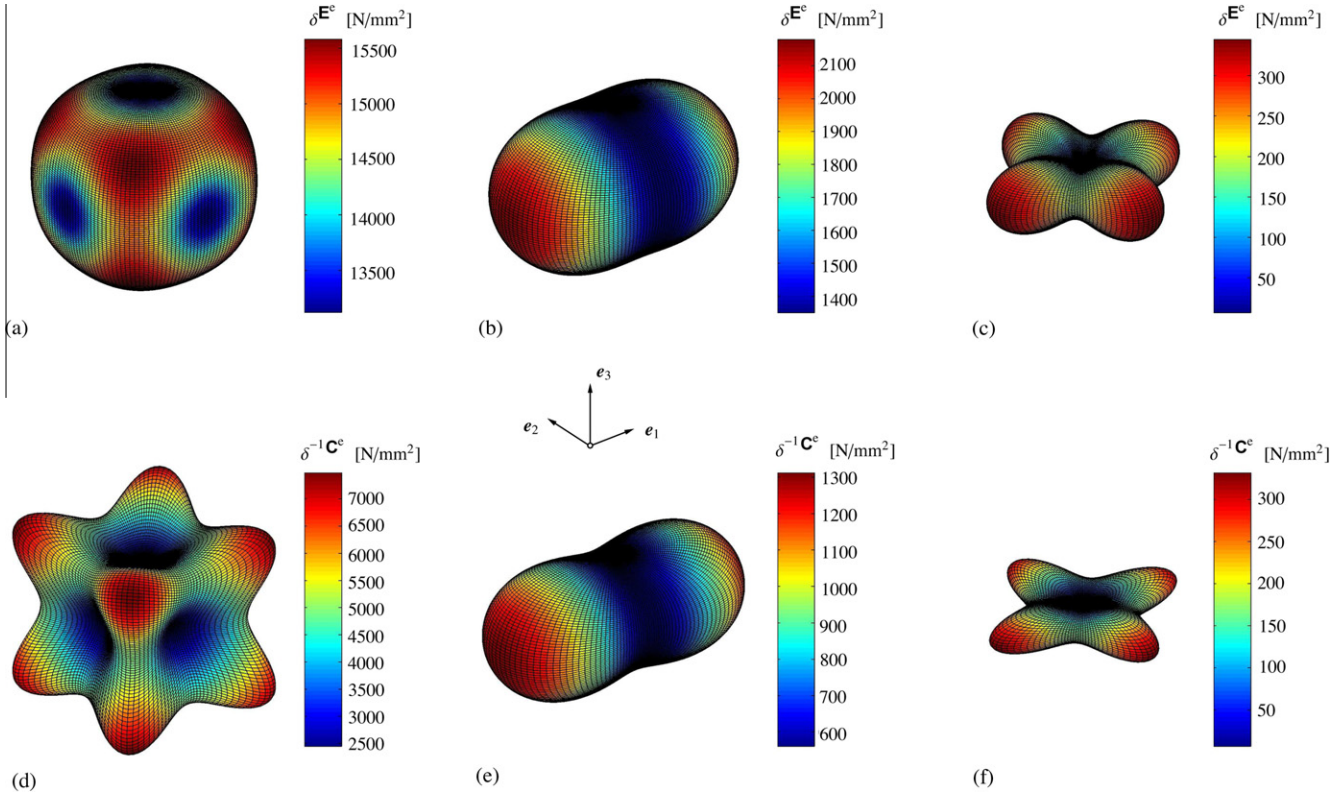


**Fig. A.15.** Visualisation of anisotropy by odf-type surface plots based on fourth-order elasticity and compliance tensors; upper row (a–c) based on  $\mathbf{E}^e$ , lower row (d–f) based on  $\mathbf{C}^e$ . Coefficients of  $\mathbf{E}^e$  in Voigt notation, superscript v: (a,d) Cubic symmetry with  $E_{11}^{ev} = 13120$ ,  $E_{12}^{ev} = 11450$ ,  $E_{44}^{ev} = 2680$ , cf. Ma et al. (2008). (b,e) Transverse isotropy with  $E_{11}^{ev} = 2180$ ,  $E_{33}^{ev} = 1350$ ,  $E_{44}^{ev} = 375$ ,  $E_{12}^{ev} = 1010$ ,  $E_{23}^{ev} = 1000$ . (c,f) Orthotropy with  $E_{11}^{ev} = 344.87$ ,  $E_{22}^{ev} = 344.87$ ,  $E_{33}^{ev} = 6.92$ ,  $E_{44}^{ev} = 59.24$ ,  $E_{55}^{ev} = 30.94$ ,  $E_{66}^{ev} = 30.94$ ,  $E_{12}^{ev} = -67.575$ ,  $E_{23}^{ev} = 0.37$ ,  $E_{13}^{ev} = 0.37$ . Units in  $[\text{N}/\text{mm}^2]$ .

equatorial plane by viewing from the south pole; see Fig. A.14 for an illustration of the  $m = 21$  integration scheme used in this paper. In Fig. A.14 we emphasise two exemplary integration directions: the intersection point of the lines connecting the integration points on the sphere and the south pole with the equatorial plane are the stereographic projected points sought. The related micro-densities  $\rho_0^i$  can be visualised by a contour-plot as shown in Fig. 5.

#### A.2. Orientation distribution function related to higher-order moments

Apart from applying the method of stereographic projection, we also make use of two different orientation distribution function-type (odf) representations. To this end, we introduce generalised structural tensors or rather higher-order density moments. The scalar moment of zeroth order is introduced as

$$A = \langle \rho_0 \rangle \approx \sum_{i=1}^m \rho_0^i w^i \quad (\text{A.1})$$

and can be interpreted as a measure of the macroscopic density. The moment of second-order reads

$$\mathbf{A} = 3 \langle \rho_0 \mathbf{r} \otimes \mathbf{r} \rangle \approx 3 \sum_{i=1}^m \rho_0^i w^i \mathbf{r}^i \otimes \mathbf{r}^i, \quad (\text{A.2})$$

whereas the moment of fourth order is represented by

$$\mathbf{A} = 5 \langle \rho_0 \mathbf{r} \otimes \mathbf{r} \otimes \mathbf{r} \otimes \mathbf{r} \rangle \approx 5 \sum_{i=1}^m \rho_0^i w^i \mathbf{r}^i \otimes \mathbf{r}^i \otimes \mathbf{r}^i \otimes \mathbf{r}^i. \quad (\text{A.3})$$

Taking into account the identities

$$\langle 1 \rangle = 1, \quad (\text{A.4})$$

$$\langle \mathbf{r} \otimes \mathbf{r} \rangle = \frac{1}{3} \mathbf{I}, \quad (\text{A.5})$$

$$\langle \mathbf{r} \otimes \mathbf{r} \otimes \mathbf{r} \otimes \mathbf{r} \rangle = \frac{1}{3} \left[ \mathbf{I}^{\text{vol}} + \frac{2}{5} \mathbf{I}^{\text{dev}} \right], \quad (\text{A.6})$$

we normalise each of these quantities such that an initially isotropic setting at  $t = 0$ , i.e.,  $\rho_0^i = \rho_0^*$  results in

$$\mathbf{A}|_{t_0} = \rho_0^* \mathbf{I}, \quad (\text{A.7})$$

$$\mathbf{A}|_{t_0} = \rho_0^* \mathbf{I}, \quad (\text{A.8})$$

$$\mathbf{A}|_{t_0} = \rho_0^* \left[ \frac{5}{3} \mathbf{I}^{\text{vol}} + \frac{2}{3} \mathbf{I}^{\text{dev}} \right]. \quad (\text{A.9})$$

Herein,  $\mathbf{I}$  denotes the second-order identity tensor, and the volumetric and deviatoric fourth-order identity tensors are represented by  $\mathbf{I}^{\text{vol}} = \frac{1}{3} \mathbf{I} \otimes \mathbf{I}$  and  $\mathbf{I}^{\text{dev}} = \mathbf{I}^{\text{sym}} - \mathbf{I}^{\text{vol}}$  with  $\mathbf{I}^{\text{sym}} = \frac{1}{2} [\mathbf{I} \otimes \mathbf{I} + \mathbf{I} \otimes \mathbf{I}]$  the fourth-order symmetric identity tensor, cf. Bažant and Oh (1985) and Lubarda and Krajcinovic (1993).

In order to compute a graphical representation of these higher-order density moments, we parametrise unit vectors  $\mathbf{r} \in \mathbb{U}^2$  in terms of spherical coordinates, for example

$$\mathbf{r}(\theta, \varphi) = \sin(\theta) \cos(\varphi) \mathbf{e}_1 + \sin(\theta) \sin(\varphi) \mathbf{e}_2 + \cos(\theta) \mathbf{e}_3. \quad (\text{A.10})$$

This allows to calculate scalar odf-type quantities, which in case of the second-order moment result in

$$\rho_0^A(\mathbf{A}, \mathbf{r}) = \mathbf{r} \cdot \mathbf{A} \cdot \mathbf{r}, \quad (\text{A.11})$$

and for the fourth-order moment we similarly introduce

$$\rho_0^A(\mathbf{A}, \mathbf{r}) = [\mathbf{r} \otimes \mathbf{r}] : \mathbf{A} : [\mathbf{r} \otimes \mathbf{r}]. \quad (\text{A.12})$$

Isotropic material properties, in other words  $\mathbf{A} \propto \mathbf{I}$  and  $\mathbf{A} \propto \mathbf{I}^{\text{sym}}$ , are represented by purely spherical distributions so that  $\rho_0^{\mathbf{A}}$  and  $\rho_0^{\mathbf{A}}$  are independent of  $\mathbf{r}$ . Odf-type representations of fourth-order tensorial quantities are well-established in the context of so-called Young's modulus plots; see Kocks et al. (2000). The underlying fourth-order tensors to visualise the materials' anisotropy are the elasticity tensor  $\mathbf{E}^e$  and the corresponding compliance tensor  $\mathbf{C}^e = [\mathbf{E}^e]^{-1}$ . By analogy with Eq. (A.11) we obtain the odf-type quantities

$$\delta \mathbf{E}^e(\mathbf{E}^e, \mathbf{r}) = [\mathbf{r} \otimes \mathbf{r}] : \mathbf{E}^e : [\mathbf{r} \otimes \mathbf{r}], \quad (\text{A.13})$$

see Fig. A.15(a-c), and

$$\delta^{-1} \mathbf{C}^e(\mathbf{C}^e, \mathbf{r}) = [[\mathbf{r} \otimes \mathbf{r}] : \mathbf{C}^e : [\mathbf{r} \otimes \mathbf{r}]]^{-1}, \quad (\text{A.14})$$

see Fig. A.15(e-f). Note that Eq. (A.13) represents solely components of the elasticity tensor, whereas Equations (A.14) reflects directional Young's modulus properties; see Cazzani and Rovati (2003) and Böhlke and Brüggemann (2001) for more background information and in view of the calculation of the compliance tensor as the inverse of the elasticity tensor in Voigt notation the reader is referred to Nemat-Nasser and Hori (1993).

Since higher-order moments include more information on the materials' anisotropic properties with increasing tensorial order, odf-type plots related to fourth-order moments show a more pronounced anisotropic shape than those related to second-order moments; see Fig. 5. In view of the moment of second order, we additionally perform a spectral decomposition,

$$\mathbf{A} = \sum_{j=1}^3 A_j \mathbf{n}_j \otimes \mathbf{n}_j \quad \text{with } \mathbf{n}_i \cdot \mathbf{n}_j = \delta_{ij}, \quad (\text{A.15})$$

to introduce a scalar measure of anisotropy defined by the difference between the largest and smallest principal value of  $\mathbf{A}$ , i.e.,  $A_1 - A_3$ ; see Fig. 8. In case of an isotropic or rather spherical distribution, all principal values of  $\mathbf{A}$  turn out to coincide so that  $A_1 - A_3 = 0$ . A spectral decomposition can also be applied to the fourth-order density moment  $\mathbf{A}$ , see Kocks et al. (2000), which is not applied in this work.

## References

- Alastrué, V., Martínez, M., Doblaré, M., Menzel, A., 2009. Anisotropic micro-sphere-based finite elasticity applied to blood vessel modelling. *Journal of the Mechanics and Physics of Solids* 57, 178–203.
- Alastrué, V., Martínez, M., Menzel, A., Doblaré, M., 2009. On the use of non-linear transformations for the evaluation of anisotropic rotationally symmetric directional integrals. Application to the stress analysis in fibred soft tissues. *International Journal for Numerical Methods in Engineering* 79, 474–504.
- Ambrosi, D., Ateshian, G., Arruda, E., Cowin, S., Dumais, J., Goriely, A., Holzapfel, G., Humphrey, J., Kemker, R., Kuhl, E., Olberding, J., Taber, L., Garikipati, K., 2011. Perspectives on biological growth and remodeling. *Journal of the Mechanics and Physics of Solids* 59, 863–883.
- Ashman, R., Rho, J., Turner, C., 1989. Anatomical variation of orthotropic elastic moduli of the proximal human tibia. *Journal of Biomechanics* 22, 895–900.
- Baliunas, A., Hurwitz, D., Ryals, A., Karrar, A., Case, J., Block, J., Andriacchi, T., 2002. Increased knee joint loads during walking are present in subjects with knee osteoarthritis. *Osteoarthritis and Cartilage* 10, 573–579.
- Bažant, Z., Oh, B., 1985. Microplane Model for Progressive Fracture of Concrete and Rock. *Journal of Engineering Mechanics* 111, 559–582.
- Bažant, Z., Oh, B., 1986. Efficient numerical integration on the surface of a sphere. *Zeitschrift für angewandte Mathematik und Mechanik* 66, 37–49.
- Beaupré, G., Orr, T., Carter, D., 1990. An approach for time-dependent bone modelling and remodelling. *Journal of Orthopaedic Research* 8, 651–670.
- Böhlke, T., Brüggemann, C., 2001. Graphical representation of the generalized Hooke's law. *Technische Mechanik* 21, 145–158.
- Carpenter, R.D., Carter, D.R., 2010. Computational simulation of spontaneous bone straightening in growing children. *Biomechanics and Modeling in Mechanobiology* 9, 317–328.
- Carter, D., Hayes, W., 1977. Compressive behavior of bone as a 2-phase porous structure. *Journal of Bone and Joint Surgery* 59, 954–962.
- Carter, D., Orr, T., Fyhrie, D., 1989. Relationships between loading history and femoral cancellous bone architecture. *Journal of Biomechanics* 22, 231–244.
- Carter, D.R., Beaupré, G.S., 2001. *Skeletal Function and Form: Mechanobiology of Skeletal Development, Aging, and Regeneration*. Cambridge University Press.
- Cazzani, A., Rovati, M., 2003. Extrema of Young's modulus for cubic and transversely isotropic solids. *International Journal of Solids and Structures* 40, 1713–1744.
- Coelho, P., Fernandes, P., Rodrigues, H., Cardoso, J., Guedes, J., 2009. Numerical modeling of bone tissue adaptation—a hierarchical approach for bone apparent density and trabecular structure. *Journal of Biomechanics* 42, 830–837.
- Coelho, P.G., Fernandes, P.R., Guedes, J.M., Rodrigues, H.C., 2008. A hierarchical model for concurrent material and topology optimisation of three-dimensional structures. *Structural and Multidisciplinary Optimization* 35, 107–115.
- Cowin, S., 1985. The relationship between the elasticity tensor and the fabric tensor. *Mechanics of Materials* 4, 137–147.
- Cowin, S., Doty, S., 2007. *Tissue Mechanics*. Springer.
- Cowin, S., Hegedus, D., 1976. Bone remodelling I: Theory of adaptive elasticity. *Journal of Elasticity* 6, 313–326.
- Cowin, S.C., 1986. Wolff's Law of Trabecular Architecture at Remodeling Equilibrium. *Journal of Biomechanical Engineering* 108, 83–88.
- Doblaré, M., García, J., 2002. Anisotropic bone remodelling model based on a continuum damage-repair theory. *Journal of Biomechanics* 35, 1–17.
- Ehret, A.E., Itskov, M., Schmid, H., 2010. Numerical integration on the sphere and its effect on the material symmetry of constitutive equations – a comparative study, microplane. *International Journal for Numerical Methods in Engineering* 81, 189–206.
- Fernandes, P., Rodrigues, H., Jacobs, C., 1999. A model of bone adaptation using a global optimisation criterion based on the trajectorial theory of Wolff. *Computer Methods in Biomechanics and Biomedical Engineering* 2, 125–138.
- García, J.M., Doblaré, M., Cegoñino, J., 2002. Bone remodelling simulation: a tool for implant design. *Computational Materials Science* 25, 100–114.
- García, J.M., Martínez, M.A., Doblaré, M., 2001. An anisotropic internal-external bone adaptation model based on a combination of CAO and continuum damage mechanics technologies. *Computer Methods in Biomechanics and Biomedical Engineering* 4, 355–377.
- Gitman, I., Askes, H., Kuhl, E., Aifantis, E., 2010. Stress concentrations in fractured compact bone simulated with a special class of anisotropic gradient elasticity. *International Journal of Solids and Structures* 47, 1099–1107.
- Göktepe, S., Abilez, O.J., Kuhl, E., 2010. A generic approach towards finite growth with examples of athlete's heart, cardiac dilation, and cardiac wall thickening. *Journal of the Mechanics and Physics of Solids* 58, 1661–1680.
- Göktepe, S., Miehe, C., 2005. A micro-macro approach to rubber-like materials. Part III: The micro-sphere model of anisotropic Mullins-type damage. *Journal of the Mechanics and Physics of Solids* 53, 2259–2283.
- Goldstein, S., 1987. The mechanical properties of trabecular bone: dependence on anatomic location and function. *Journal of Biomechanics* 20, 1055–1061.
- Harrigan, T., Hamilton, J., 1992. An analytical and numerical study of the stability of bone remodelling theories: dependence on microstructural stimulus. *Journal of Biomechanics* 25, 477–488. *Corrigendum* 26 (3) (1993) 365–366.
- Harrigan, T., Hamilton, J., 1993a. Bone strain sensation via transmembrane potential changes in surface osteoblasts: loading rate and microstructural implications. *Journal of Biomechanics* 26, 183–200.
- Harrigan, T., Hamilton, J., 1993b. Finite element simulation of adaptive bone remodelling: a stability criterion and a time stepping method. *International Journal for Numerical Methods in Engineering* 36, 837–854.
- Harrigan, T., Hamilton, J., 1994. Necessary and sufficient conditions for global stability and uniqueness in finite element simulations of adaptive bone remodelling. *International Journal of Solids and Structures* 31, 97–107.
- Harrysson, M., Ristinmaa, M., Wallin, M., Menzel, A., 2010. Framework for deformation induced anisotropy in glassy polymers. *Acta Mechanica* 211, 195–213.
- Hashash, Y.M.A., Yao, J.I.C., Wotring, D.C., 2003. Glyph and hyperstreamline representation of stress and strain tensors and material constitutive response. *International Journal for Numerical and Analytical Methods in Geomechanics* 27, 603–626.
- Heo, S., Xu, Y., 2001. Constructing fully symmetric cubature formulae for the sphere. *Mathematics of Computation* 70, 269–279.
- Himpel, G., Kuhl, E., Menzel, A., Steinmann, P., 2005. Computational modelling of isotropic multiplicative growth. *Computer Modeling in Engineering and Sciences* 8, 119–134.
- Himpel, G., Menzel, A., Kuhl, E., Steinmann, P., 2008. Time-dependent fibre reorientation of transversely isotropic continua—finite element formulation and consistent linearization. *International Journal for Numerical Methods in Engineering* 73, 1413–1433.
- Huiskes, R., Weinans, H., Grootenboer, H., Dalstra, M., Fudala, B., Slooff, T., 1987. Adaptive bone-remodeling theory applied to prosthetic-design analysis. *Journal of Biomechanics* 20, 1135–1150.
- Hulet, C., Sabatier, J., Souquet, D., Locker, B., Marcelli, C., Vielpeau, C., 2002. Distribution of bone mineral density at the proximal tibia in knee osteoarthritis. *Calcified Tissue International* 71, 315–322.
- Hurwitz, D., Sumner, D., Andriacchi, T., Sugar, D., 1998. Dynamic knee loads during gait predict proximal tibial bone distribution. *Journal of Biomechanics* 31, 423–430.
- Jacobs, C.R., Levenston, M.E., Beaupré, G.S., Simo, J.C., Carter, D.R., 1995. Numerical instabilities in bone remodeling simulations: the advantages of a node-based finite element approach. *Journal of Biomechanics* 28, 449–459.
- Jacobs, C.R., Simo, J.C., Beaupré, G.S., Carter, D.R., 1997. Adaptive bone remodeling incorporating simultaneous density and anisotropy considerations. *Journal of Biomechanics* 30, 603–613.
- Kanatani, K.I., 1984. Distribution of directional data and fabric tensors. *International Journal of Engineering Science* 22, 149–164.

- Kocks, U., Tomé, C., Wenk, H.R. (Eds.), 2000. *Texture and Anisotropy-Preferred Orientations in Polycrystals and their Effect on Material Properties*. Cambridge University Press.
- Kriz, R., Glaessgen, E., MacRae, J., 1995. Eigenvalue-eigenvector glyphs: visualizing zeroth, second, fourth and higher order tensors in a continuum. In: *Workshop on Modeling the Development of Residual Stresses During Thermalset Composite Curing*. University of Illinois, Champaign-Urbana.
- Krstin, N., Nackenhorst, U., Lammering, R., 2000. Zur konstitutiven Beschreibung des anisotropen beanspruchungsadaptiven Knochenbaus. *Technische Mechanik* 20, 31–40.
- Kuhl, E., Maas, R., Himpel, G., Menzel, A., 2007. Computational modeling of arterial wall growth. *Biomechanics and Modeling in Mechanobiology* 6, 321–331.
- Kuhl, E., Menzel, A., Garikipati, K., 2006. On the convexity of transversely isotropic chain network models. *Philosophical Magazine* 86, 3241–3258.
- Kuhl, E., Menzel, A., Steinmann, P., 2003. Computational modeling of growth – a critical review, a classification of concepts and two new consistent approaches. *Computational Mechanics* 32, 71–88.
- Kuhl, E., Ramm, E., Willam, K., 2000. Failure analysis of elasto-plastic material models on different levels of observation. *International Journal of Solids and Structures* 37, 7259–7280.
- Kuhl, E., Steinmann, P., 2003a. Mass- and volume specific views on thermodynamics for open systems. *Proceedings of the Royal Society A* 459, 2547–2568.
- Kuhl, E., Steinmann, P., 2003b. Theory and numerics of geometrically non-linear open system mechanics. *International Journal for Numerical Methods in Engineering* 58, 1593–1615.
- Kuhl, E., Steinmann, P., 2004. Material forces in open system mechanics. *Computer Methods in Applied Mechanics and Engineering* 193, 2357–2381.
- Kuhl, E., Steinmann, P., Carol, I., 2001. A thermodynamically consistent approach to microplane theory. Part II. Dissipation and inelastic constitutive modeling. *International Journal of Solids and Structures* 38, 2933–2952.
- Lubarda, V., Hoger, A., 2002. On the mechanics of solids with a growing mass. *International Journal of Solids and Structures* 39, 4627–4664.
- Lubarda, V., Krajcinovic, D., 1993. Damage tensors and the crack density distribution. *International Journal of Solids and Structures* 30, 2859–2877.
- Ma, D., Friák, M., Neugebauer, J., Raabe, D., Roters, F., 2008. Multiscale simulation of polycrystal mechanics of textured  $\beta$ -Ti alloys using ab initio and crystal-based finite element methods. *Physica Status Solidi (b)* 245, 2642–2648.
- Menzel, A., 2005. Modelling of anisotropic growth in biological tissues – a new approach and computational aspects. *Biomechanics and Modeling in Mechanobiology* 3, 147–171.
- Menzel, A., 2006. Anisotropic remodelling of biological tissues. In: Holzapfel, G., Ogden, R. (Eds.), *Mechanics of Biological Tissue*. Springer, pp. 91–104.
- Menzel, A., 2007. A fibre reorientation model for orthotropic multiplicative growth – configurational driving stresses, kinematics-based reorientation, and algorithmic aspects. *Biomechanics and Modeling in Mechanobiology* 6, 303–320.
- Menzel, A., Harrysson, M., Ristinmaa, M., 2008. Towards an orientation-distribution-based multi-scale approach for remodelling biological tissues. *Computer Methods in Biomechanics and Biomedical Engineering* 11, 505–524.
- Menzel, A., Waffenschmidt, T., 2009. A micro-sphere-based remodelling formulation for anisotropic biological tissues. *Philosophical Transactions of the Royal Society A* 367, 3499–3523.
- Menzel, A., Waffenschmidt, T., Alastrué, V., 2010. An anisotropic micro-sphere approach applied to the modelling of soft biological tissues. In: Kreiss, G., Lötstedt, P., Målqvist, A., Neytcheva, M. (Eds.), *Numerical Mathematics and Advanced Applications*. Springer, pp. 637–644.
- von Meyer, H., 1867. Die Architektur der Spongiosa. *Reichert's und Du Bois Reymold's Archiv für Anatomie und Physiologie* 34, 615–628.
- Miehe, C., Göktepe, S., 2005. A micro–macro approach to rubber-like materials. Part II: The micro–sphere model of rubber viscoelasticity. *Journal of the Mechanics and Physics of Solids* 53, 2231–2258.
- Miehe, C., Göktepe, S., Lulei, F., 2004. A micro-macro approach to rubber-like materials – Part I: the non-affine micro-sphere model of rubber elasticity. *Journal of the Mechanics and Physics of Solids* 52, 2617–2660.
- Moreo, P., Pérez, M., García-Aznar, J., Doblaré, M., 2007. Modelling the mechanical behaviour of living bony interfaces. *Computer Methods in Applied Mechanics and Engineering* 196, 3300–3314.
- Nackenhorst, U., Krstin, N., Lammering, R., 2000. A constitutive law for anisotropic stress adaptive bone remodeling. *ZAMM Journal of Applied Mathematics and Mechanics/ Zeitschrift für Angewandte Mathematik und Mechanik* 80, 399–400.
- Nemat-Nasser, S., Hori, M., 1993. *Micromechanics: Overall Properties of Heterogeneous Materials*. Applied Mathematics and Mechanics. Elsevier.
- Pang, H., Shiwalkar, A., Madomo, C., Taylor, R., Andriacchi, T., Kuhl, E., 2012. Computational modeling of bone density profiles in response to gait: a subject-specific approach. *Biomechanics and Modeling in Mechanobiology* 11, 379–390.
- Pettermann, H., Reiter, T., Rammerstorfer, F., 1997. Computational simulation of internal bone remodeling. *Archives of Computational Methods in Engineering* 4, 295–323.
- Reina-Romo, E., Gómez-Benito, M.J., García-Aznar, J.M., Domínguez, J., Doblaré, M., 2010. Growth mixture model of distraction osteogenesis: effect of pre-traction stresses. *Biomechanics and Modeling in Mechanobiology* 9, 103–115.
- Rho, J.Y., Kuhn-Spearing, L., Zioupos, P., 1998. Mechanical properties and the hierarchical structure of bone. *Medical Engineering & Physics* 20, 92–102.
- Rodrigues, H., Jacobs, C., Guedes, J.M., Bendsø, M.P., 2002. Global and local material optimization models applied to anisotropic bone adaptation. In: Pedersen, P., Bendsø, M.P. (Eds.), *IUTAM Symposium on Synthesis in Bio Solid Mechanics, Solid Mechanics and Its Applications*, vol. 69. Springer, Netherlands, pp. 209–220.
- Taber, L., 1995. *Biomechanics of growth, remodelling, and morphogenesis*. American Society of Mechanical Engineers – Applied Mechanics Reviews 48, 487–545.
- Taylor, R.E., Zheng, C., Jackson, R.P., Doll, J.C., Chen, J.C., Holzbaur, K.R.S., Besier, T., Kuhl, E., 2009. The phenomenon of twisted growth: humeral torsion in dominant arms of high performance tennis players. *Computer Methods in Biomechanics and Biomedical Engineering* 12, 83–93.
- Waffenschmidt, T., Menzel, A., 2012. Application of an anisotropic growth and remodelling formulation to computational structural design. *Mechanics Research Communications*. <http://dx.doi.org/10.1016/j.mechrescom.2011.12.004>.
- Weinans, H., Huiskes, R., Grootenboer, H., 1992. The behavior of adaptive bone-remodeling simulation models. *Journal of Biomechanics* 25, 1425–1441.
- Weng, S., 1998. Ein anisotropes Knochenbaumodell und dessen Anwendung. *Technische Mechanik* 18, 173–180.
- Williams, J.L., Lewis, J.L., 1982. Properties and an anisotropic model of cancellous bone from the proximal tibial epiphysis. *Journal of Biomechanical Engineering* 104, 50–56.
- Wolff, J., 1870. Ueber die innere Architectur der Knochen und ihre Bedeutung für die Frage vom Knochenwachstum. *Virchows Archiv für Pathologische Anatomie und Physiologie und für Klinische Medizin* 50, 389–453.
- Wolff, J., 1892. *Das Gesetz der Transformation der Knochen*. Hirschwald, Berlin.
- Zhang, J., Michalenko, M., Kuhl, E., Ovaert, T., 2010. Characterization of indentation response and stiffness reduction of bone using a continuum damage model. *Journal of the Mechanical Behavior of Biomedical Materials* 3, 189–202.
- Zysset, P., Curnier, A., 1995. An alternative model for anisotropic elasticity based on fabric tensors. *Mechanics of Materials* 21, 243–250. See also Technical Note by Cowin, S.C., 1998. *Journal of Biomechanics* 31, 759–762.